Chapter 6

Two-Dimensional Problems

In this chapter we apply the MoM to scattering problems involving two-dimensional structures. The discussion and examples illustrate the approach outlined in Section 3.6.3.1, the practical computation of the matrix elements (3.188–3.193), and the choice of basis and testing functions. We first consider conducting objects, and discuss the implementation of the $\mathcal{L}$ and $\hat{\mathbf{n}}\times\mathcal{K}$ operators in the EFIE and nMFIE. We then consider dielectric objects and the $\mathcal{K}$ operator in the EFIE/MFIE, and the $\hat{\mathbf{n}}\times\mathcal{L}$ operator in the nMFIE. Because general two-dimensional problems can be split into TM- and TE-polarized sub-problems, we consider each polarization individually.

6.1 Conducting Objects

We begin with conducting objects and the solution of the EFIE and nMFIE in both TM and TE polarization. As the $\mathcal{L}$ operator is valid on thin open structures, the EFIE is first applied to a thin conducting strip of finite length and the necessary self-term expressions are derived. The EFIE is then generalized to a cylindrical contour of arbitrary shape. As the $\hat{\mathbf{n}}\times\mathcal{K}$ operator is valid only on closed surfaces, the nMFIE is considered only for closed cylindrical geometries.

6.1.1 Physical Optics Approximation for Conductors

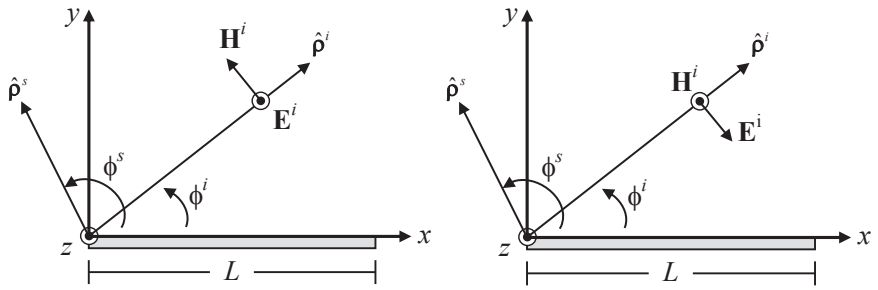
Consider again the equivalent problem in Figure 3.2c, with surface currents given by (3.152) and (3.153). If we assume that the object is very electrically large, at any point on the surface, it can be treated as locally planar and infinite in extent. If the object is perfectly conducting, $\mathbf{M}_1(\mathbf{r}) = 0$ and the scattered magnetic field is equal in amplitude and phase to the incident field. The electric surface current on the exterior is then

$$\mathbf{J}_{\mathrm{PO}}(\mathbf{r}) = 2\,\hat{\mathbf{n}}\times\mathbf{H}^i(\mathbf{r})\,, \tag{6.1}$$

which is known as the physical optics (PO) approximation for conductors. PO assumes that the currents exist only on directly illuminated surfaces, and are zero in shadowed

areas. We will compare the results from PO and the MoM for several objects in this section. We will then consider PO in significantly more detail in a later chapter.

6.1.2 EFIE: TM Polarization



(a) TM Polarization (b) TE Polarization

Figure 6.1: Thin Strip

Consider a thin, perfectly conducting strip illuminated by a TM-polarized plane wave as illustrated in Figure 6.1a. The incident electric field has unit amplitude, and is given by

$$\mathbf{E}^i(\boldsymbol{\rho}) = e^{jk\hat{\boldsymbol{\rho}}_i\cdot\boldsymbol{\rho}}\,\hat{\mathbf{z}} = e^{jk(x\cos\phi^i + y\sin\phi^i)}\,\hat{\mathbf{z}}\,, \tag{6.2}$$

where $\hat{\boldsymbol{\rho}}^i = \cos\phi^i\hat{\mathbf{x}} + \sin\phi^i\hat{\mathbf{y}}$. In the absence of magnetic current, the EFIE (3.181) is

$$j\omega\mu\big[(\mathcal{L}\mathbf{J}_l)(\mathbf{r})\big]_{tan} = \big[\mathbf{E}^i_l(\mathbf{r})\big]_{tan}\,. \tag{6.3}$$

On the thin strip this becomes

$$j\omega\mu\Big[1 + \frac{1}{k^2}\nabla\nabla\cdot\Big]\int_0^L \mathbf{J}(x')\,G(\boldsymbol{\rho},\boldsymbol{\rho}')\,dx' = e^{jkx\cos\phi^i}\hat{\mathbf{z}}\,, \tag{6.4}$$

where the integration is only in x' as the strip is very thin. Substituting the two-dimensional Green's function (3.49) and using the identity (3.79) then yields

$$\frac{\omega\mu}{4}\int_0^L \mathbf{J}(x')\,H_0^{(2)}\big(k|x-x'|\big)\,dx' = e^{jkx\cos\phi^i}\hat{\mathbf{z}}\,, \tag{6.5}$$

where since the electric field (and the induced current) has only a $\hat{\mathbf{z}}$ component, $\nabla'\cdot\mathbf{J}(x') = 0$ and only the first term remains. Once $\mathbf{J}(x')$ is known, the scattered far electric field (3.145) can then be computed as

$$\mathbf{E}^s(\boldsymbol{\rho}) = -\omega\mu\sqrt{\frac{j}{8\pi k}}\,\frac{e^{-jk\rho}}{\sqrt{\rho}}\int_0^L \mathbf{J}(x')\,e^{jkx'\cos\phi^s}\,dx'\,. \tag{6.6}$$

The corresponding Physical Optics current on the strip is

$$\mathbf{J}_{\rm PO}(x) = \frac{2}{\eta}\,\hat{\mathbf{y}}\times\Big[-\hat{\boldsymbol{\rho}}^i\times\mathbf{E}^i(\boldsymbol{\rho})\Big] = \frac{2}{\eta}\sin\phi^i e^{jkx\cos\phi^i}\hat{\mathbf{z}}\,. \tag{6.7}$$

6.1.2.1 PEC Strip Solution Using Pulse Functions – TM Polarization

We will first solve this problem using pulse basis functions and point matching for testing. Dividing the strip into N segments of width $\Delta_x = L/N$ yields N basis functions. Point matching at the center of the testing segment x_m yields matrix elements given by

$$Z_{mn} = \int_{x_n}^{x_{n+1}} H_0^{(2)}\big(k\rho\big)\, dx' \,, \tag{6.8}$$

where $\rho = |x_m - x'|$, and the right-hand side vector elements are

$$V_m = \frac{4}{\omega\mu} e^{jkx_m \cos\phi^i} \,. \tag{6.9}$$

Note that the system matrix has a symmetric Toeplitz structure due to the choice of basis functions and the linear geometry of the strip.

6.1.2.1.1 Regular Terms

For segments that are sufficiently separated, (6.8) can be evaluated using an M-point numerical quadrature as

$$Z_{mn} = \sum_{q=1}^{M} w(x_q) H_0^{(2)}\big(k|x_m - x_q|\big) \,, \tag{6.10}$$

where x_m is at the center of the testing segment, and x_q and $w(x_q)$ are the quadrature points and weights on the source segment, respectively. For this case, we can also use a simple centroidal approximation, which is

$$Z_{mn} = \Delta_x H_0^{(2)}\big(k|x_m - x_n|\big) \,, \tag{6.11}$$

where x_m and x_n are located at the centers of the source and testing segments, respectively.

6.1.2.1.2 Self Terms

On overlapping segments, the Hankel function has an integrable singularity. To handle this, we will perform a singularity extraction. To do so, we use the small argument approximation to the Hankel function, which is

$$H_0^{(2)}(k\rho) \approx 1 - j\frac{2}{\pi}\Big[\log\Big(\frac{k\rho}{2}\Big) + \gamma\Big] \qquad k\rho \to 0 \,, \tag{6.12}$$

where $\gamma \approx 0.5772$ is Euler's constant. Adding and subtracting this term to (6.8) yields

$$\begin{aligned} Z_{mm} = &\int_0^{\Delta_x} \left[H_0^{(2)}\big(k\rho\big) - 1 + j\frac{2}{\pi}\Big(\log\Big(\frac{k\rho}{2}\Big) + \gamma\Big)\right] dx' \\ &+ \int_0^{\Delta_x} \left[1 - j\frac{2}{\pi}\left(\log\left(\frac{k\rho}{2}\right) + \gamma\right)\right] dx' \,. \end{aligned} \tag{6.13}$$

where $\rho = |x_m - x'|$, but x_m is measured from the start of the source segment. The integrand of the first term is now bounded, so it can be evaluated numerically. The second term is evaluated analytically, and is

$$I_s(x_m) = \left(1 - j\frac{2\gamma}{\pi}\right)\int_0^{\Delta_x} dx' - j\frac{2}{\pi}\int_0^{\Delta_x} \log\left(\frac{k}{2}|x_m - x'|\right) dx' \,. \tag{6.14}$$

The solution is [1]

$$I_s(x_m) = \Delta_x\left(1 - j\frac{2\gamma}{\pi}\right) - j\frac{2}{\pi}\left[(\Delta_x - x_m)\log\left(\frac{k|\Delta_x - x_m|}{2}\right) + x_m\log\left(\frac{k|x_m|}{2}\right) - \Delta_x\right] , \tag{6.15}$$

which is valid for all values of x_m. For overlapping segments, $x_m = \Delta_x/2$, and (6.15) evaluates to

$$I_s\left(x_m = \frac{\Delta_x}{2}\right) = \Delta_x\left(1 - j\frac{2}{\pi}\left[\gamma + \log\left(\frac{k\Delta_x}{4}\right) - 1\right]\right) \,. \tag{6.16}$$

6.1.2.1.3 Near Terms

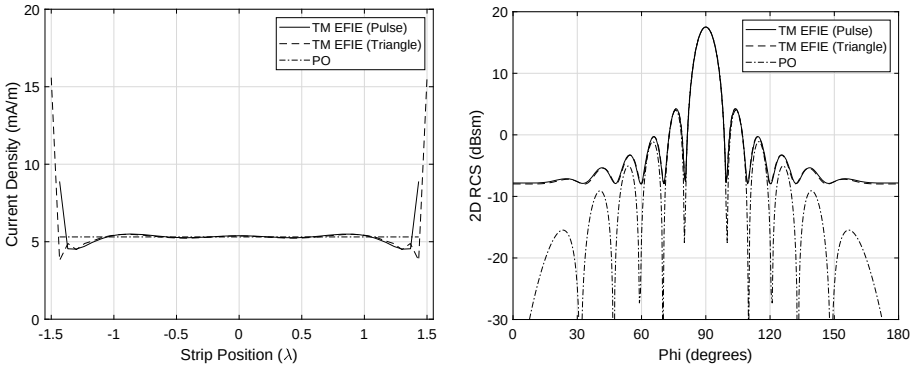
When segments are nearby but not overlapping, the integrand can still exhibit singular behavior, leading to inaccuracies if (6.11) is used. In this case, we can again use the singularity extraction technique in (6.13), where the analytic portion is now given by (6.15).

We note that due to the linear geometry of the strip, it is possible to use (6.13) to compute all the matrix elements. However, evaluation of near terms can be time consuming for more complicated problems, particularly in the 3D case (Chapter 8). Thus, we restrict our use of near-term expressions only to distances where they are needed to meet the required accuracy.

6.1.2.1.4 Numerical Results

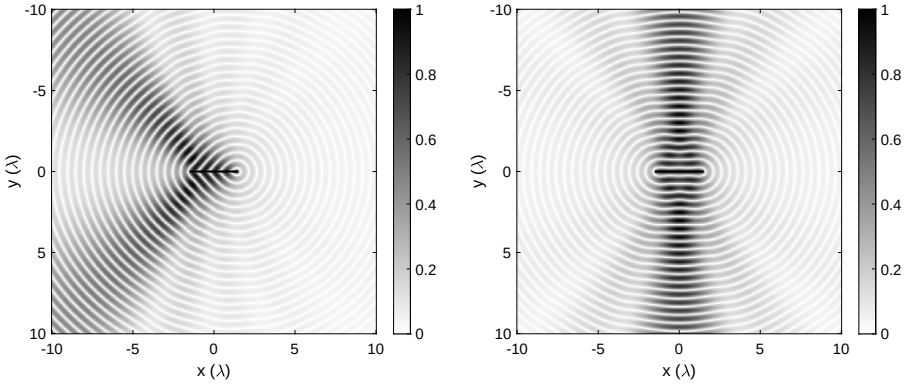
Consider a strip of width 3λ centered at the origin, divided into 45 segments (15 segments/λ). In Figure 6.2a, we plot the induced surface current amplitude at broadside incidence ($\phi^i = \pi/2$). The current is singular near the edges, and the magnitude falls off quickly with distance from each edge. To this we compare the PO current of (6.7), which agrees well with the EFIE near the center of the strip, but poorly at the edges. In Figure 6.2b we plot the 2D RCS for incident angles from 0 to 180 degrees. PO compares well to the EFIE at angles near broadside and within the main lobe, but poorly beyond that. This is because edge diffraction is significant at these angles, and those effects are omitted by PO.

Using (3.120) and the computed currents, we next compute the scattered near field in a $20\lambda \times 20\lambda$ region around the strip. The normalized real component of the electric field is shown (in V/m) for $\phi^i = \pi/4$ and $\phi^i = \pi/2$ in Figures 6.3a and 6.3b, respectively.



(a) Induced Surface Current ($\phi^i = \pi/2$) (b) 2D Monostatic RCS ($0 \leq \phi^i \leq \pi$)

Figure 6.2: 3λ Strip: Currents and RCS, TM Polarization



(a) $\phi^i = \pi/4$ (b) $\phi^i = \pi/2$

Figure 6.3: Scattered TM Near Field ($|\operatorname{Re}(\mathbf{E})|$, V/m) of 3λ Strip (Pulse Solution)

6.1.2.2 PEC Strip Solution Using Triangle Functions – TM Polarization

We next solve this problem using triangle basis and testing functions. As the current has only a $\hat{\mathbf{z}}$-component, we omit the vector notation and work with their scalar components, which we refer to as f_m and f_n, respectively. The strip is again divided into N segments of width $\Delta_x = L/N$. As the current does not vanish at the ends, we use $N-1$ whole triangle functions and a half-triangle function at each end, yielding $N+1$ unknowns. The matrix elements are

$$Z_{mn} = \int_{f_m} f_m(x) \int_{f_n} f_n(x')\, H_0^{(2)}\big(k\rho\big)\, dx'\, dx\,, \tag{6.17}$$

where $\rho = |x - x'|$. For segments that are sufficiently separated, we evaluate (6.17)

using an M-point numerical quadrature over the source and testing triangles, yielding

$$Z_{mn} = \sum_{p=1}^{M} w(x_p)\, f_m(x_p) \sum_{q=1}^{M} w(x_q)\, f_n(x_q)\, H_0^{(2)}\big(k|x_p - x_q|\big)\,, \tag{6.18}$$

where x_q and x_p are the source and quadrature points, respectively. Likewise, the right-hand side vector elements are evaluated as

$$V_m = \frac{4}{\omega\mu}\int_{f_m} f_m(x) e^{jkx\cos\phi^i}\, dx \;= \frac{4}{\omega\mu}\sum_{p=1}^{M} w(x_p) f_m(x_p) e^{jkx_p\cos\phi^i}\,. \tag{6.19}$$

6.1.2.2.1 Self Terms

When the source and testing segments overlap, an integrable singularity occurs in the Hankel function. To address this, we evaluate the innermost integral in (6.17) numerically and analytically, and the outermost integral numerically. For the innermost integral, we use the same approach as with the pulse functions. Referring to (6.13), the inner part of (6.17) can be written as

$$\begin{aligned} I(x_p) = &\int_0^{\Delta_x} f_n(x') \left[H_0^{(2)}(k\rho) - 1 + j\frac{2}{\pi}\left(\log\left(\frac{k\rho}{2}\right) + \gamma\right)\right] dx' \\ &+ \int_0^{\Delta_x} f_n(x') \left[1 - j\frac{2}{\pi}\left(\log\left(\frac{k\rho}{2}\right) + \gamma\right)\right] dx'\,, \end{aligned} \tag{6.20}$$

where $\rho = |x_p - x'|$, but x_p is measured from the start of the source segment. The integrand of the first term is now bounded, and can be evaluated numerically.

The second term is evaluated analytically. To begin, we note that on each segment, there are two half-triangle functions, $f_1(x') = 1 - x'/\Delta_x$ (having negative slope), and $f_2(x') = x'/\Delta_x$ (having positive slope). We begin by evaluating the integral involving $f_2(x)$. Following (6.14), this can be written as

$$\frac{1}{\Delta_x}\left(1 - j\frac{2\gamma}{\pi}\right)\int_0^{\Delta_x} x'\, dx' - j\frac{2}{\pi}\frac{1}{\Delta_x}\int_0^{\Delta_x} x' \log\left(\frac{k}{2}|x_m - x'|\right) dx'\,. \tag{6.21}$$

The solution is [1]

$$\begin{aligned} I_s(x_p) = &\frac{\Delta_x}{2}\left(1 - j\frac{2\gamma}{\pi}\right) \\ &-j\frac{2}{\pi\Delta_x}\left[\frac{\Delta_x^2 - x_m^2}{2}\log\left(\frac{k|\Delta_x - x_m|}{2}\right) + \frac{x_m^2}{2}\log\left(\frac{k|x_m|}{2}\right) - \frac{\Delta_x^2}{4} - \frac{x_m\Delta_x}{2}\right]\,. \end{aligned} \tag{6.22}$$

The remaining integral involving involving $f_1(x)$ can be evaluated by subtracting (6.22) from (6.15).

6.1.2.2.2 Near Terms

Due to the linear geometry of the strip, we can also use the self term expressions to compute the near terms. Although lengthy, they are straightforward to implement.

6.1.2.2.3 Numerical Results

We again consider the 3λ strip, using 45 segments, and a 5-point Gaussian quadrature on each segment. In Figure 6.2a is shown the computed surface current at broadside incidence. As triangle basis functions were used, the currents are defined at the segment endpoints instead of the centers. The differences in amplitude at the ends of the strip are noticeable. In Figure 6.2b is shown the 2D RCS, which agrees quite well with the pulse basis solution at all angles.

6.1.3 Generalized EFIE: TM Polarization

Consider now a two-dimensional conducting contour C of arbitrary shape, shown in Figure 6.4. Following (6.4) and (6.5), the EFIE (3.181) on C can be generalized for TM polarization as

$$\frac{\omega\mu}{4}\int_C \mathbf{J}(\boldsymbol{\rho}')\, H_0^{(2)}\big(k|\boldsymbol{\rho}-\boldsymbol{\rho}'|\big)\, d\boldsymbol{\rho}' = \mathbf{E}^i(\boldsymbol{\rho})\,. \tag{6.23}$$

6.1.3.1 MoM Discretization

The contour C is divided into a number of linear segments, and the current $\mathbf{J}(\boldsymbol{\rho})$ is expanded using $\hat{\mathbf{z}}$-oriented electric basis functions $\mathbf{f}^z$. Testing with these same functions

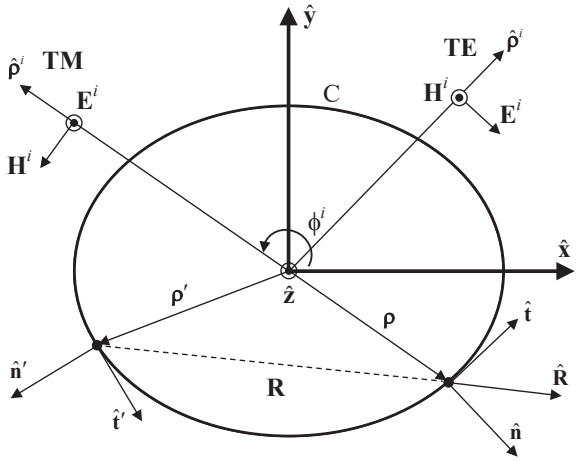


Figure 6.4: 2D Contour: TM and TE Polarization

yields the matrix elements (3.188) for the TM case, given by

$$Z_{mn}^{EJ} = \frac{\omega\mu}{4} \mathrm{L}^{zz}(\mathbf{f}_m^z, \mathbf{f}_n^z) \,, \tag{6.24}$$

where

$$\mathrm{L}^{zz}(\mathbf{f}_m^z, \mathbf{f}_n^z) = \int_{\mathbf{f}_m^z} \mathbf{f}_m^z(\boldsymbol{\rho}) \cdot \int_{\mathbf{f}_n^z} \mathbf{f}_n^z(\boldsymbol{\rho}') \; H_0^{(2)}\big(k|\boldsymbol{\rho} - \boldsymbol{\rho}'|\big) \; d\boldsymbol{\rho}' \; d\boldsymbol{\rho} \,. \tag{6.25}$$

The right-hand side vector elements (3.194) are

$$V_m^{E,TM} = \int_{\mathbf{f}_m^z} \mathbf{f}_m^z(\boldsymbol{\rho}) \cdot \mathbf{E}_z^i(\boldsymbol{\rho}) \; d\boldsymbol{\rho} \,. \tag{6.26}$$

6.1.3.2 General Solution Using Triangle Functions

Using triangle basis and testing functions, (6.25) can be evaluated on non-overlapping segments using an M-point numerical quadrature, yielding

$$\mathrm{L}^{zz}(\mathbf{f}_m^z, \mathbf{f}_n^z) = \sum_{p=1}^{M} w(\boldsymbol{\rho}_p) f_m^z(\boldsymbol{\rho}_p) \sum_{q=1}^{M} w(\boldsymbol{\rho}_q) f_n^z(\boldsymbol{\rho}_q) \; H_0^{(2)}\big(k|\boldsymbol{\rho}_p - \boldsymbol{\rho}_q|\big) \,, \tag{6.27}$$

where we have again omitted the vector notation for convenience. Self-terms are evaluated using the procedure outlined in Section 6.1.2.2.1. When generating the matrix elements, (6.27) is evaluated efficiently using a loop over segment pairs and the resulting values placed into the corresponding matrix locations. As each segment supports at most two triangles, it contributes to up to four matrix elements. The right-hand side vector elements (6.26) are then

$$V_m^{E,TM} = \sum_{p=1}^{M} w(\boldsymbol{\rho}_p) f_m^z(\boldsymbol{\rho}_p) E_z^i(\boldsymbol{\rho}_p) \,. \tag{6.28}$$

For an incident plane wave with an electric field of unit amplitude, (6.28) becomes

$$V_m^{E,TM} = \sum_{p=1}^{M} w(x_p) f_m^z(x_p) e^{jk(x_p \cos\phi_i + y_p \sin\phi_i)} \,. \tag{6.29}$$

6.1.4 EFIE: TE Polarization

We next consider the thin strip for TE polarization, as illustrated in Figure 6.1b, where an incident electric field of unit amplitude is now given by

$$\mathbf{E}^i(\boldsymbol{\rho}) = (\sin\phi^i \hat{\mathbf{x}} - \cos\phi^i \hat{\mathbf{y}}) e^{jk(x\cos\phi^i + y\sin\phi^i)} \,. \tag{6.30}$$

As the incident field has $\hat{\mathbf{x}}$ and $\hat{\mathbf{y}}$ components, the induced electric currents will as well. However, since $\hat{\mathbf{y}}$-directed currents (normal to the strip) cannot exist in this case, the current has only an $\hat{\mathbf{x}}$ component. Therefore, (3.181) can be written as

$$\int_0^L J_x(x')\left[1+\frac{1}{k^2}\frac{\partial^2}{\partial x^2}\right]H_0^{(2)}(k\rho)\,dx' = \frac{4}{\omega\mu}\sin\phi^i e^{jkx\cos\phi^i}\ , \tag{6.31}$$

where $\rho=\sqrt{(x-x')^2+(y-y')^2}$. Let us now evaluate the expression

$$\left[1+\frac{1}{k^2}\frac{\partial^2}{\partial x^2}\right]H_0^{(2)}(k\rho)\ . \tag{6.32}$$

To begin, we note the recurrence relation [2]

$$\frac{d}{du}H_n^{(2)}(u) = -H_{n+1}^{(2)}(u)+\frac{n}{u}H_n^{(2)}(u)\ , \tag{6.33}$$

and so

$$\frac{d}{du}H_0^{(2)}(u) = -H_1^{(2)}(u)\ , \tag{6.34}$$

and

$$\frac{\partial}{\partial x}H_0^{(2)}(k\rho) = \frac{d}{du}\left[H_0^{(2)}(u)\right]\frac{\partial u}{\partial x} = -H_1^{(2)}(u)\frac{\partial u}{\partial x}\ , \tag{6.35}$$

where $u=k\rho$. Therefore,

$$\frac{\partial u}{\partial x} = \frac{\partial(k\rho)}{\partial x} = \frac{k(x-x')}{\rho}\ , \tag{6.36}$$

and so

$$\frac{\partial}{\partial x}H_0^{(2)}(k\rho) = -H_1^{(2)}(k\rho)\frac{k(x-x')}{\rho}\ . \tag{6.37}$$

Differentiating a second time yields

$$\frac{\partial^2}{\partial x^2}H_0^{(2)}(k\rho) = -\frac{k(x-x')}{\rho}\left[\frac{\partial}{\partial x}H_1^{(2)}(k\rho)\right]-H_1^{(2)}(k\rho)\left[\frac{\partial}{\partial x}\frac{k(x-x')}{\rho}\right]\ , \tag{6.38}$$

which is

$$\frac{\partial^2}{\partial x^2}H_0^{(2)}(k\rho) = -\frac{k^2(x-x')^2}{\rho^2}\left[-H_2^{(2)}(k\rho)+\frac{1}{k\rho}H_1^{(2)}(k\rho)\right]-H_1^{(2)}(k\rho)\left[\frac{k}{\rho}-\frac{k(x-x')^2}{\rho^3}\right]\ . \tag{6.39}$$

The second and fourth term cancel, leaving

$$\frac{\partial^2}{\partial x^2}H_0^{(2)}(k\rho) = \frac{k^2(x-x')^2}{\rho^2}H_2^{(2)}(k\rho)-\frac{k}{\rho}H_1^{(2)}(k\rho)\ . \tag{6.40}$$

Using the recurrence relationship [2]

$$\frac{2}{k\rho}H_1^{(2)}(k\rho) = H_0^{(2)}(k\rho)+H_2^{(2)}(k\rho)\ , \tag{6.41}$$

we can then write

$$\left[1+\frac{1}{k^2}\frac{\partial^2}{\partial x^2}\right]H_0^{(2)}(k\rho)=\frac{1}{2}\left[\frac{2(x-x')^2}{\rho^2}-1\right]H_2^{(2)}(k\rho)+\frac{1}{2}H_0^{(2)}(k\rho)\,. \quad (6.42)$$

We note from the geometry of Figure 6.1b that

$$\cos\theta=\frac{(x-x')}{\sqrt{(x-x')^2+(y-y')^2}}=\frac{(x-x')}{\rho}\,, \quad (6.43)$$

where the angle θ is measured in the right-hand sense from the positive x axis. Using this, and the double-angle formula $\cos(2\theta)=2\cos^2\theta-1$, the previous expression can be written as

$$\left[1+\frac{1}{k^2}\frac{\partial^2}{\partial x^2}\right]H_0^{(2)}(k\rho)=\frac{1}{2}\Big[\cos(2\theta)H_2^{(2)}(k\rho)+H_0^{(2)}(k\rho)\Big]\,, \quad (6.44)$$

and we can now write (6.31) as

$$\frac{1}{2}\int_0^L J_x(x')\Big[\cos(2\theta)H_2^{(2)}(k\rho)+H_0^{(2)}(k\rho)\Big]\,dx'=\frac{4}{\omega\mu}\sin\phi^i e^{jkx\cos\phi^i}\,. \quad (6.45)$$

Note that for observations on the strip, $\rho=|x-x'|$, and for any point x' where $x'\neq x$, θ is either 0 or π, thus $\cos(2\theta)=1$. In these cases, (6.41) can be used to write (6.45) as

$$\int_0^L J_x(x')\,\frac{H_1^{(2)}(k\rho)}{k\rho}\,dx'=\frac{4}{\omega\mu}\sin\phi^i e^{jkx\cos\phi^i}\,. \quad (6.46)$$

The corresponding PO current on the strip for the TE case is

$$\mathbf{J}_{\rm PO}(\boldsymbol{\rho})=2\,\hat{\mathbf{n}}\times\mathbf{H}^i(\boldsymbol{\rho})=\frac{2}{\eta}\,e^{jkx\cos\phi^i}\hat{\mathbf{x}}\,, \quad (6.47)$$

which at broadside incidence is equivalent in magnitude to the PO current for the TM case.

6.1.4.1 PEC Strip Solution Using Pulse Functions – TE Polarization

We will solve this problem using pulse basis functions and point matching for testing. Dividing the strip into N segments of width $\Delta_x=L/N$ yields N basis functions. Point matching at the center of the testing segment x_m yields matrix elements given by

$$Z_{mn}=\int_{x_n}^{x_{n+1}}\frac{H_1^{(2)}(k\rho)}{k\rho}\,dx'\,, \quad (6.48)$$

where $\rho=|x_m-x'|$, and the right-hand side vector elements are

$$V_m=\frac{4}{\omega\mu}\sin\phi^i e^{jkx_m\cos\phi^i}\,. \quad (6.49)$$

6.1.4.1.1 Regular Terms

For segments that are not close, we compute the matrix elements using a centroidal approximation of (6.46), which is

$$Z_{mn} = \Delta_x \frac{H_1^{(2)}(k\rho)}{k\rho} = \Delta_x \frac{H_1^{(2)}\left(k|x_m - x_n|\right)}{k|x_m - x_n|} \,, \tag{6.50}$$

where x_m and x_n are located at the centers of the testing and source segments, respectively.

6.1.4.1.2 Near Terms

When segments are adjacent or separated by only a few segments, the kernel in (6.50) can exhibit singular behavior. We can alleviate this as we did in the TM case, by performing a singularity extraction. To do so, we use the small argument approximation to the Hankel function, which is [2]

$$H_1^{(2)}(k\rho) \approx \frac{k\rho}{2} + \frac{2j}{\pi k\rho} \qquad k\rho \to 0 \,, \tag{6.51}$$

and so,

$$\frac{H_1^{(2)}(k\rho)}{k\rho} \approx \frac{1}{2} + \frac{2j}{\pi(k\rho)^2} \qquad k\rho \to 0 \tag{6.52}$$

Adding and subtracting this term to (6.48) yields matrix elements given by

$$Z_{mn} = \int_0^{\Delta_x} \left[\frac{H_1^{(2)}(k\rho)}{k\rho} - \frac{1}{2} - \frac{2j}{\pi(k\rho)^2} \right] dx' + \int_0^{\Delta_x} \left[\frac{1}{2} + \frac{2j}{\pi(k\rho)^2} \right] dx' \tag{6.53}$$

where $P = |x_m - x'|$, but x_m is measured from the start of the source segment. The integrand of the first term is now much smoother, and can be evaluated numerically. The second term is evaluated analytically, and is

$$I_s(x_m) = \int_0^{\Delta_x} \left[\frac{1}{2} + \frac{2j}{\pi(k\rho)^2} \right] dx' = \frac{\Delta_x}{2} + \frac{2j}{\pi k^2} \int_0^{\Delta_x} \frac{1}{|x_m - x'|^2} dx' \,. \tag{6.54}$$

The solution is [1]

$$I_s(x_m) = \Delta_x \left[\frac{1}{2} + \frac{2j}{\pi k^2} \frac{1}{x_m(x_m - \Delta_x)} \right] \,. \tag{6.55}$$

Note that (6.55) is only valid when x_m lies outside the source segment.

6.1.4.1.3 Self Terms

For the self terms, we will need to work with (6.45). For the part involving $H_0^{(2)}(k\rho)$, we can use the results from (6.13), but we must treat the part involving $H_2^{(2)}(k\rho)$ carefully, as it has a non-integrable singularity. In this case, we will move the observation point off of the strip, perform the integration, and then apply a limiting argument as the point approaches the strip. The integral to be evaluated is

$$I = \int_{-\Delta_x/2}^{\Delta_x/2} \cos(2\theta) H_2^{(2)}(k\rho)\, dx' \tag{6.56}$$

where the testing point $x_m = 0$, and we have again used the double-angle formula for $\cos(2\theta)$. As before, we perform a singularity extraction, where the small argument approximation to the Hankel function $H_2^{(2)}(k\rho)$ is [2]

$$H_2^{(2)}(k\rho) \approx \frac{(k\rho)^2}{8} + \frac{j}{\pi} + \frac{4j}{\pi(k\rho)^2} \qquad k\rho \to 0\ . \tag{6.57}$$

We see that it is the last term that is singular. So, now adding and subtracting this term to (6.56), and using the expression for $\cos(2\theta)$ from (6.43), we write the integral as

$$I = \int_0^{\Delta_x} \cos(2\theta) \left[H_2^{(2)}(k\rho) - \frac{4j}{\pi(k\rho)^2} \right] dx' + 2 \int_0^{\Delta_x/2} \cos(2\theta) \frac{4j}{\pi(k\rho)^2}\, dx' \tag{6.58}$$

The first term is bounded and can be integrated numerically, where

$$H_2^{(2)}(k\rho) - \frac{4j}{\pi(k\rho)^2} \approx \frac{(k\rho)^2}{8} + \frac{j}{\pi} \qquad k\rho \to 0\ , \tag{6.59}$$

and the second term is evaluated analytically. To do so, we set the observation point $(x, y) = (0, a)$, where a is very small. The distance ρ is then

$$\rho = \sqrt{(x')^2 + a^2}\ . \tag{6.60}$$

Using the expressions for $\cos(2\theta)$ from (6.43), we write the second integral as

$$I_s = j\frac{16}{\pi k^2} \int_0^{\Delta_x/2} \left[\frac{(x')^2}{\rho^4} - \frac{1}{2\rho^2} \right] dx'\ . \tag{6.61}$$

Substituting in ρ from above, this becomes

$$I_s = \frac{8j}{\pi k^2} \int_0^{\Delta_x/2} \frac{(x')^2 - a^2}{[(x')^2 + a^2]^2} dx'\ , \tag{6.62}$$

which evaluates to [1]

$$I_s = -\frac{16j}{\pi k^2} \frac{\Delta_x}{\Delta_x^2 + 4a^2}\ . \tag{6.63}$$

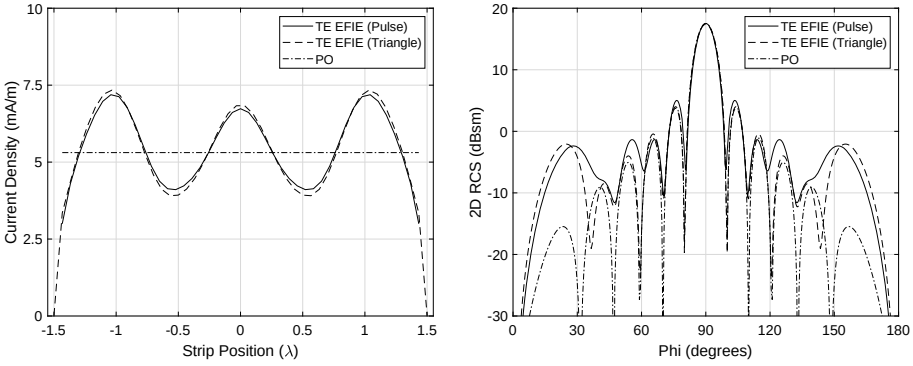
Finally, letting $a \to 0$, we obtain

$$I_s = -\frac{16j}{\pi k^2 \Delta_x}\ . \tag{6.64}$$

6.1.4.1.4 Numerical Results

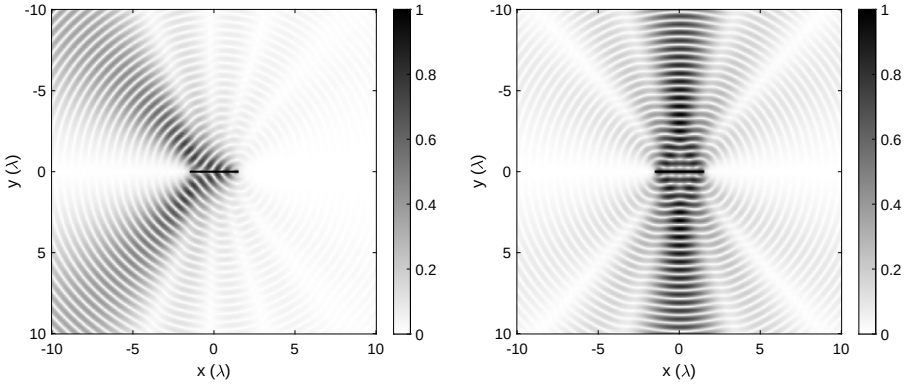
In Figure 6.5a is shown the amplitude of the computed surface current on the 3λ strip at broadside incidence, using 45 segments. As the current is $\hat{\boldsymbol{x}}$-oriented, it tends toward zero near the ends of the strip, as expected. To this we compare the PO current of (6.47), which compares poorly to the EFIE. In Figure 6.5b we compare the 2D RCS obtained from the EFIE to that of PO. Again, PO does well near normal incidence, but poorly beyond that.

Using (3.120) and the computed currents, we next compute the scattered near field in a $20\lambda \times 20\lambda$ region around the strip. The normalized real component of the electric field is shown (in V/m) for $\phi^i = \pi/4$ and $\phi^i = \pi/2$ in Figures 6.6a and 6.6b, respectively.



(a) Induced Surface Current ($\phi^i = \pi/2$) (b) 2D Monostatic RCS ($0 \leq \phi^i \leq \pi$)

Figure 6.5: 3λ Strip: Currents and RCS, TE Polarization



(a) $\phi^i = \pi/4$ (b) $\phi^i = \pi/2$

Figure 6.6: Scattered TE Near Field ($|\,\mathrm{Re}(\mathbf{E})|$, V/m) of 3λ Strip (Pulse Solution)

6.1.5 Generalized EFIE: TE Polarization

As in the TM case, the EFIE (3.181) on a conducting contour C can be generalized for TE polarization as

$$\frac{\omega\mu}{4}\int_C \left[1+\frac{1}{k^2}\nabla\nabla\cdot\right]\mathbf{J}(\boldsymbol{\rho}')H_0^{(2)}\big(k|\boldsymbol{\rho}-\boldsymbol{\rho}'|\big)\,d\boldsymbol{\rho}' = \mathbf{E}^i(\boldsymbol{\rho})\,, \tag{6.65}$$

where $\mathbf{J}(\boldsymbol{\rho})$ is everywhere tangent to C.

6.1.5.1 MoM Discretization

Contour C is divided into a number of linear segments, and the current $\mathbf{J}(\boldsymbol{\rho})$ expanded using vector basis functions that are tangent to each segment. Testing with those same functions yields the matrix elements (3.188) for the TE case, which are

$$Z_{mn}^{EJ} = \frac{\omega\mu}{4}\mathrm{L}^{tt}(\mathbf{f}_m^t,\mathbf{f}_n^t)\,, \tag{6.66}$$

where

$$\begin{aligned}\mathrm{L}^{tt}(\mathbf{f}_m^t,\mathbf{f}_n^t) = &\int_{\mathbf{f}_m^t}\mathbf{f}_m^t(\boldsymbol{\rho})\cdot\int_{\mathbf{f}_n^t}\mathbf{f}_n^t(\boldsymbol{\rho}')\,H_0^{(2)}\big(k|\boldsymbol{\rho}-\boldsymbol{\rho}'|\big)\,d\boldsymbol{\rho}'\,d\boldsymbol{\rho}\\ &+\frac{1}{k^2}\int_{\mathbf{f}_m^t}\mathbf{f}_m^t(\boldsymbol{\rho})\cdot\int_{\mathbf{f}_n^t}\nabla\nabla\cdot\Big[\mathbf{f}_n^t(\boldsymbol{\rho}')\,H_0^{(2)}\big(k|\boldsymbol{\rho}-\boldsymbol{\rho}'|\big)\Big]\,d\boldsymbol{\rho}'\,d\boldsymbol{\rho}\,.\end{aligned} \tag{6.67}$$

and the right-hand side vector elements (3.194) are

$$V_m^{E,TE} = \int_{\mathbf{f}_m^t}\mathbf{f}_m^t(\boldsymbol{\rho})\cdot\mathbf{E}^i(\boldsymbol{\rho})\,d\boldsymbol{\rho}\,. \tag{6.68}$$

Note that if we apply the differential operators in the second term directly, they act on the Green's function in much the same way as in Pocklington's Equation (5.13). This makes the analysis much more complicated, as we saw in Section 6.1.4, and it compounds the singularity of the Hankel function, making an accurate solution much more difficult. If the basis and testing functions have a well-behaved divergence, we can instead re-distribute the differential operators following (3.207), as we did with the thin wire EFIE in Section 5.5. Doing so allows us to rewrite (6.67) as

$$\begin{aligned}\mathrm{L}^{tt}(\mathbf{f}_m^t,\mathbf{f}_n^t) = &\int_{\mathbf{f}_m^t}\mathbf{f}_m^t(\boldsymbol{\rho})\cdot\int_{\mathbf{f}_n^t}\mathbf{f}_n^t(\boldsymbol{\rho}')\,H_0^{(2)}\big(k|\boldsymbol{\rho}-\boldsymbol{\rho}'|\big)\,d\boldsymbol{\rho}'\,d\boldsymbol{\rho}\\ &-\frac{1}{k^2}\int_{\mathbf{f}_m^t}\nabla\cdot\mathbf{f}_m^t(\boldsymbol{\rho})\int_{\mathbf{f}_n^t}\nabla'\cdot\mathbf{f}_n^t(\boldsymbol{\rho}')\,H_0^{(2)}\big(k|\boldsymbol{\rho}-\boldsymbol{\rho}'|\big)\,d\boldsymbol{\rho}'\,d\boldsymbol{\rho}\,.\end{aligned} \tag{6.69}$$

6.1.5.2 General Solution Using Triangle Functions

The geometry in the TE case is similar to the thin-wire problem of Section 5.5.2, and so the orientation of the basis and testing functions follows that of Figure 5.4. We can

evaluate (6.69) on non-overlapping segments using an M-point numerical quadrature, yielding

$$\mathrm{L}^{tt}(\mathbf{f}_m^t, \mathbf{f}_n^t) = \sum_{p=1}^{M}\sum_{q=1}^{M} w(\boldsymbol{\rho}_p)w(\boldsymbol{\rho}_q)\left[\mathbf{f}_m^t(\boldsymbol{\rho}_p)\cdot\mathbf{f}_n^t(\boldsymbol{\rho}_q) \pm \frac{1}{k^2\Delta_l^2}\right] H_0^{(2)}\left(k|\boldsymbol{\rho}_p - \boldsymbol{\rho}_q|\right) , \tag{6.70}$$

where we have used the fact that the divergence of each triangle function is

$$\nabla\cdot\mathbf{f}^t(\boldsymbol{\rho}) = \pm\frac{1}{\Delta_l} . \tag{6.71}$$

The sign of this term depends on the orientation of the basis and testing functions on each segment. The right-hand side of (6.70) should be evaluated inside a loop over segment pairs and the resulting alues placed into the corresponding matrix locations. On overlapping segments, the self terms for (6.69) can be evaluated using the singularity extraction technique and the expressions already developed for the pulse and triangle basis functions in Sections 6.1.2.1.2 and 6.1.2.2.1, respectively.

The right-hand side vector elements are then

$$V_m^{E,TE} = \sum_{p=1}^{M} w(\boldsymbol{\rho}_p)\,\mathbf{f}_m^t(\boldsymbol{\rho}_p)\cdot\mathbf{E}^i(\boldsymbol{\rho}_p) , \tag{6.72}$$

and for an incident plane wave with an electric field of unit amplitude, (6.72) is

$$V_m^{E,TE} = \sum_{p=1}^{M} w(\boldsymbol{\rho}_p)\,\mathbf{f}_m^t(\boldsymbol{\rho}_p)\cdot(\sin\phi^i\hat{\mathbf{x}} - \cos\phi^i\hat{\mathbf{y}})e^{jk(x_p\cos\phi^i + y_p\sin\phi^i)} . \tag{6.73}$$

6.1.5.3 PEC Strip Solution Using Triangle Functions – TE Polarization

We now solve the problem of the PEC strip for TE polarization, shown in Figure 6.1b, using triangle basis and testing functions. As in the TM case, the strip is divided into N segments of width $\Delta_x = L/N$, and we use $N-1$ whole triangle functions and a half-triangle function at each end, for $N+1$ total unknowns. The MoM matrix and right-hand side vectors are computed following Section 6.1.5.2.

6.1.5.3.1 Numerical Results

In Figure 6.5a is shown the computed surface current at broadside incidence using triangle functions, compared to the previous results using pulse basis functions and point matching, and the PO approximation. The currents obtained using triangle functions go to zero on the ends of the strip, however those obtained from pulse basis functions do not. In Figure 6.2b is shown the 2D RCS, where the comparison between the pulse and triangle basis functions is good near broadside, but less so at more oblique angles.

6.1.6 Generalized nMFIE: TM Polarization

Given the TM-polarized incident field of (6.2), the corresponding magnetic field is

$$\mathbf{H}^i(\boldsymbol{\rho}) = -\frac{1}{\eta}\,\hat{\boldsymbol{\rho}}^i \times \mathbf{E}^i(\boldsymbol{\rho}) = \frac{1}{\eta}\,(-\sin\phi^i\hat{\mathbf{x}} + \cos\phi^i\hat{\mathbf{y}})\; e^{jk(x\cos\phi^i + y\sin\phi^i)}\;. \quad (6.74)$$

Using (3.49) and (3.94), the nMFIE (3.183) can be written on the conducting contour C in Figure 6.4 as

$$\frac{1}{2}\mathbf{J}(\boldsymbol{\rho}) - \frac{j}{4}\,\hat{\mathbf{n}}(\boldsymbol{\rho}) \times \int_{C'} \mathbf{J}(\boldsymbol{\rho}') \times \nabla H_0^{(2)}(k\rho)\; d\boldsymbol{\rho}' = \hat{\mathbf{n}}(\boldsymbol{\rho}) \times \mathbf{H}^i(\boldsymbol{\rho})\;, \quad (6.75)$$

where we have used the notation C' to indicate the integration is not valid for $\boldsymbol{\rho} = \boldsymbol{\rho}'$. Using the fact that

$$\nabla H_0^{(2)}(k\rho) = -k\left[\frac{x-x'}{R}\hat{\mathbf{x}} + \frac{y-y'}{R}\hat{\mathbf{y}}\right] H_1^{(2)}(k\rho) = -k\,\hat{\mathbf{R}}(\boldsymbol{\rho},\boldsymbol{\rho}')H_1^{(2)}(k\rho)\;, \quad (6.76)$$

where

$$\hat{\mathbf{R}}(\boldsymbol{\rho},\boldsymbol{\rho}') = \frac{x-x'}{R}\hat{\mathbf{x}} + \frac{y-y'}{R}\hat{\mathbf{y}} = \frac{\boldsymbol{\rho}-\boldsymbol{\rho}'}{|\boldsymbol{\rho}-\boldsymbol{\rho}'|}\;, \quad (6.77)$$

we can write (6.75) as

$$\frac{1}{2}\mathbf{J}(\boldsymbol{\rho}) + \frac{jk}{4}\hat{\mathbf{n}}(\boldsymbol{\rho}) \times \int_{C'} \mathbf{J}(\boldsymbol{\rho}') \times \hat{\mathbf{R}}(\boldsymbol{\rho},\boldsymbol{\rho}')\; H_1^{(2)}(k\rho)\; d\boldsymbol{\rho}' = \hat{\mathbf{n}}(\boldsymbol{\rho}) \times \mathbf{H}^i(\boldsymbol{\rho})\;. \quad (6.78)$$

The TM CFIE is formed by combining the TM EFIE (6.23) and the TM nMFIE (6.78) following (3.184).

6.1.6.0.1 MoM Discretization

The contour C is divided into a number of linear segments, and the current $\mathbf{J}(\boldsymbol{\rho})$ is expanded using $\hat{\mathbf{z}}$-oriented electric basis functions. Testing with these same functions yields the matrix elements (3.192) for the TM case, which are

$$Z_{mn}^{nHJ} = \mathrm{nK}^{zz}(\mathbf{f}_m^z, \mathbf{f}_n^z)\;, \quad (6.79)$$

where

$$\mathrm{nK}^{zz}(\mathbf{f}_m^z, \mathbf{f}_n^z) = \frac{1}{2}\int_{\mathbf{f}_m^z = \mathbf{f}_n^z} \mathbf{f}_m^z(\boldsymbol{\rho}) \cdot \mathbf{f}_n^z(\boldsymbol{\rho})\; d\boldsymbol{\rho} + \frac{jk}{4}\int_{\mathbf{f}_m^z} \mathbf{f}_m^z(\boldsymbol{\rho}) \cdot \hat{\mathbf{n}}(\boldsymbol{\rho}) \times \int_{\mathbf{f}_n^z} \mathbf{f}_n^z(\boldsymbol{\rho}') \times \hat{\mathbf{R}}(\boldsymbol{\rho},\boldsymbol{\rho}')\; H_1^{(2)}(k\rho)\; d\boldsymbol{\rho}'\; d\boldsymbol{\rho}\;. \quad (6.80)$$

The first term in (6.80) is evaluated over boundary segments where $\mathbf{f}_m^z$ and $\mathbf{f}_n^z$ overlap, and the second where they do not. If we use the vector identity

$$\mathbf{A} \times \mathbf{B} \times \mathbf{C} = (\mathbf{A}\cdot\mathbf{C})\mathbf{B} - (\mathbf{A}\cdot\mathbf{B})\mathbf{C}\;, \quad (6.81)$$

and the fact that $\hat{\mathbf{n}}(\boldsymbol{\rho}) \cdot \mathbf{f}_n^z(\boldsymbol{\rho}') = 0$, we can write

$$\hat{\mathbf{n}}(\boldsymbol{\rho}) \times \mathbf{f}_n^z(\boldsymbol{\rho}') \times \hat{\mathbf{R}}(\boldsymbol{\rho}, \boldsymbol{\rho}') = \mathbf{f}_n^z(\boldsymbol{\rho}') \Big[\hat{\mathbf{n}}(\boldsymbol{\rho}) \cdot \hat{\mathbf{R}}(\boldsymbol{\rho}, \boldsymbol{\rho}') \Big] \,. \tag{6.82}$$

This allows us to write (6.80) as

$$\begin{aligned} \mathrm{nK}^{zz}(\mathbf{f}_m^z, \mathbf{f}_n^z) = \frac{1}{2} \int_{\mathbf{f}_m^z = \mathbf{f}_n^z} \mathbf{f}_m^z(\boldsymbol{\rho}) \cdot \mathbf{f}_n^z(\boldsymbol{\rho}) \, d\boldsymbol{\rho} + \frac{jk}{4} \int_{\mathbf{f}_m^z} \mathbf{f}_m^z(\boldsymbol{\rho}) \cdot \\ \int_{\mathbf{f}_n^z} \mathbf{f}_n^z(\boldsymbol{\rho}') \Big[\hat{\mathbf{n}}(\boldsymbol{\rho}) \cdot \hat{\mathbf{R}}(\boldsymbol{\rho}, \boldsymbol{\rho}') \Big] \, H_1^{(2)}(k\rho) \, d\boldsymbol{\rho}' \, d\boldsymbol{\rho} \,. \end{aligned} \tag{6.83}$$

The right-hand side vector elements (3.196) are

$$V_m^{nH,TM} = \int_{\mathbf{f}_m^z} \mathbf{f}_m^z(\boldsymbol{\rho}) \cdot \Big[\hat{\mathbf{n}}(\boldsymbol{\rho}) \times \mathbf{H}^i(\boldsymbol{\rho}) \Big] \, d\boldsymbol{\rho} \,. \tag{6.84}$$

6.1.6.1 Solution Using Triangle Functions

Using triangle basis and testing functions, (6.83) is computed using an M-point numerical quadrature yielding

$$\begin{aligned} \mathrm{nK}^{zz}(\mathbf{f}_m^z, \mathbf{f}_n^z) = & \frac{1}{2} \sum_{p=1}^{M} w(\boldsymbol{\rho}_p) f_m^z(\boldsymbol{\rho}_p) f_n^z(\boldsymbol{\rho}_p) + \frac{jk}{4} \sum_{p=1}^{M} w(\boldsymbol{\rho}_p) f_m^z(\boldsymbol{\rho}_p) \cdot \\ & \sum_{q=1}^{M} w(\boldsymbol{\rho}_q) f_n^z(\boldsymbol{\rho}_q) (\hat{\mathbf{n}}_p \cdot \hat{\mathbf{R}}_{pq}) \, H_1^{(2)}\big(k|\boldsymbol{\rho}_p - \boldsymbol{\rho}_q|\big) \,, \end{aligned} \tag{6.85}$$

where we have again omitted the vector notation for $\mathbf{f}_m^z$ and $\mathbf{f}_n^z$. The right-hand side elements are

$$V_m^{nH,TM} = \sum_{p=1}^{M} w(\boldsymbol{\rho}_p) \, \mathbf{f}_m^z(\boldsymbol{\rho}_p) \cdot \Big[\hat{\mathbf{n}}(\boldsymbol{\rho}_p) \times \mathbf{H}^i(\boldsymbol{\rho}_p) \Big] \,. \tag{6.86}$$

For a plane wave having an electric field of unit amplitude, (6.86) becomes

$$V_m^{nH,TM} = \frac{1}{\eta} \sum_{p=1}^{M} w(\boldsymbol{\rho}_p) \, \mathbf{f}_m^z(\boldsymbol{\rho}_p) \cdot \Big[\hat{\mathbf{n}}(\boldsymbol{\rho}_p) \times (-\sin\phi^i \hat{\mathbf{x}} + \cos\phi^i \hat{\mathbf{y}}) \Big] \tag{6.87}$$

$$e^{jk(x_p \cos\phi^i + y_p \sin\phi^i)} \,. \tag{6.88}$$

6.1.7 Generalized nMFIE: TE Polarization

Consider again the conducting contour C, with a TE-polarized incident field as shown in Figure 6.4. Given the electric field of (6.30), the corresponding magnetic field is

$$\mathbf{H}^i(\boldsymbol{\rho}) = -\frac{1}{\eta} \, \hat{\boldsymbol{\rho}}^i \times \mathbf{E}^i(\boldsymbol{\rho}) = \frac{1}{\eta} \, e^{jk(x \cos\phi^i + y \sin\phi^i)} \, \hat{\mathbf{z}} \,. \tag{6.89}$$

The nMFIE for the TE case is written identically to (6.78). However, as the induced current $\mathbf{J}(\boldsymbol{\rho})$ is tangent to C, the simplications made during the MoM discretization for the TM case do not apply in the TE case.

The TE CFIE can be created by combining the TE EFIE (6.65) and the TE nMFIE (6.78) following (3.184).

6.1.7.0.1 MoM Discretization

We again divide the boundary C into N segments, and the current $\mathbf{J}(\boldsymbol{\rho})$ is expanded using electric basis functions that are tangent to C. Testing with these same functions yields the matrix elements (3.192) for the TE case, which are

$$Z_{mn}^{nHJ} = \mathrm{nK}^{tt}(\mathbf{f}_m^t, \mathbf{f}_n^t) \;, \tag{6.90}$$

where

$$\mathrm{nK}^{tt}(\mathbf{f}_m^t, \mathbf{f}_n^t) = \frac{1}{2} \int_{\mathbf{f}_m^t = \mathbf{f}_n^t} \mathbf{f}_m^t(\boldsymbol{\rho}) \cdot \mathbf{f}_n^t(\boldsymbol{\rho}) \; d\boldsymbol{\rho} + \frac{jk}{4} \int_{\mathbf{f}_m^t} \mathbf{f}_m^t(\boldsymbol{\rho}) \cdot \hat{\mathbf{n}}(\boldsymbol{\rho}) \times \int_{\mathbf{f}_n^t} \mathbf{f}_n^t(\boldsymbol{\rho}') \times \hat{\mathbf{R}}(\boldsymbol{\rho}, \boldsymbol{\rho}') \; H_1^{(2)}(k\rho) \; d\boldsymbol{\rho}' \; d\boldsymbol{\rho} \;. \tag{6.91}$$

The first term in (6.91) is evaluated over boundary segments where $\mathbf{a}^t$ and $\mathbf{b}^t$ overlap, and the second where they do not. The right-hand side vector elements (3.196) are

$$V_m^{nH,TE} = \int_{\mathbf{f}_m^t} \mathbf{f}_m^t(\boldsymbol{\rho}) \cdot \Big[\hat{\mathbf{n}}(\boldsymbol{\rho}) \times \mathbf{H}^i(\boldsymbol{\rho}) \Big] \; d\boldsymbol{\rho} \;. \tag{6.92}$$

6.1.7.1 Solution Using Triangle Functions

The triangle basis and testing functions are oriented in the same manner as in Section 6.1.5.2. Applying an M-point numerical quadrature to (6.91) yields

$$\mathrm{nK}^{tt}(\mathbf{f}_m^t, \mathbf{f}_n^t) = \frac{1}{2} \sum_{p=1}^{M} w(\boldsymbol{\rho}_p) \; \mathbf{f}_m^t(\boldsymbol{\rho}_p) \cdot \mathbf{f}_n^t(\boldsymbol{\rho}_p) + \frac{jk}{4} \sum_{p=1}^{M} w(\boldsymbol{\rho}_p) \; \mathbf{f}_m^t(\boldsymbol{\rho}_p) \cdot \Big[\hat{\mathbf{n}}(\boldsymbol{\rho}_p) \times \sum_{q=1}^{M} w(\boldsymbol{\rho}_q) \; \mathbf{f}_n^t(\boldsymbol{\rho}_q) \times \hat{\mathbf{R}}_{pq} \; H_1^{(2)}\big(k|\boldsymbol{\rho}_p - \boldsymbol{\rho}_q|\big) \Big], \tag{6.93}$$

and right-hand side vector elements are

$$V_m^{nH,TE} = \sum_{p=1}^{M} w(\boldsymbol{\rho}_p) \; \mathbf{f}_m^t(\boldsymbol{\rho}_p) \cdot \Big[\hat{\mathbf{n}}(\boldsymbol{\rho}_p) \times \mathbf{H}^i(\boldsymbol{\rho}_p) \Big] \;. \tag{6.94}$$

For a plane wave having an electric field of unit amplitude, (6.94) becomes

$$V_m^{nH,TE} = \frac{1}{\eta} \sum_{p=1}^{M} w(\boldsymbol{\rho}_p) \; \mathbf{f}_m^t(\boldsymbol{\rho}_p) \cdot \Big[\hat{\mathbf{n}}(\boldsymbol{\rho}_p) \times \hat{\mathbf{z}} \Big] e^{jk(x_p \cos\phi^i + y_p \sin\phi^i)} \;. \tag{6.95}$$

Note that many of the vectors in the above expressions are constant on a segment, and can be moved outside the summations where appropriate.

6.1.8 Examples

We will now use the generalized EFIE and nMFIE to analyze the scattering of plane waves by a two-dimensional conducting circular cylinder for TM and TE polarizations. The integral equation solution uses the MoM discretizations formulated via triangle basis and testing functions.

6.1.8.1 Conducting Cylinder: TM Polarization

For TM polarization, the exact solution for the scattered electric field of a conducting cylinder is [3] (4.1-2)

$$E_z^s(\rho,\phi^s) = \sum_{n=0}^{\infty} j^n c_n A_n H_n^{(2)}(k_0\rho)\cos(n\phi^s) \;, \tag{6.96}$$

where $|E_z^i| = 1$ for convenience, $\phi^i = 0$, and ϕ^s is the bistatic scattering angle, and $c_n = 1$ for $n = 0$, and $c_n = 2$ otherwise. For the conducting cylinder, the coefficients A_n are [3] (4.1-13)

$$A_n = -\frac{J_n(k_0 a)}{H_n^{(2)}(k_0 a)} \;, \tag{6.97}$$

where a is the radius of the cylinder. The scattered far electric field is [3] (4.1-5)

$$E_z^s(\rho,\phi^s) = \sqrt{\frac{2}{\pi}}\frac{e^{-j(k_0\rho-\pi/4)}}{\sqrt{k_0\rho}}\sum_{n=0}^{\infty}(-1)^n c_n A_n \cos n\phi^s \;. \tag{6.98}$$

The induced electric current $J_z(\phi^a)$ is [3] (4.1-15)

$$J_z(\phi^a) = \frac{2}{\pi\eta_0 k_0 a}\sum_{n=0}^{\infty}\frac{j^n c_n \cos n\phi^a}{H_n^{(2)}(k_0 a)} \;, \tag{6.99}$$

where ϕ^a is the azimuthal angle on the surface of the cylinder. In the high-frequency limit ($k_0 a \to \infty$), the RCS in the backscattering direction ($\phi^s = 0$) approaches πa, and in the forward-scattering direction ($\phi^s = \pi$), it approaches $4k_0 a^2$ [3].

Noting that on the cylinder, $\hat{\mathbf{n}} = \hat{\boldsymbol{\rho}} = \cos\phi^a\ \hat{\mathbf{x}} + \sin\phi^a\ \hat{\mathbf{y}}$, for angles ϕ^a in the illuminated region the PO current (6.74) is then

$$J_z^{\mathrm{PO}}(\phi^a) = \frac{2}{\eta}(\cos\phi^a\cos\phi^i + \sin\phi^a\sin\phi^i)e^{jk(x\cos\phi^i + y\sin\phi^i)} \;, \tag{6.100}$$

and in the shadowed region, $J_z^{\mathrm{PO}}(\phi^a) = 0$.

6.1.8.1.1 MoM Linear System

For the TM case, the MoM linear system can be written as

$$\left[\alpha\frac{\omega\mu_0}{4}\mathrm{L}^{zz} + (1-\alpha)\eta_0\mathrm{nK}^{zz}\right][J^z] = \left[\alpha V^{E,z} + (1-\alpha)\eta_0 V^{nH,z}\right] \;. \tag{6.101}$$

For $0 < \alpha < 1$, this comprises the CFIE formulation. For $\alpha = 1$, it is the EFIE, and for $\alpha = 0$, the nMFIE.

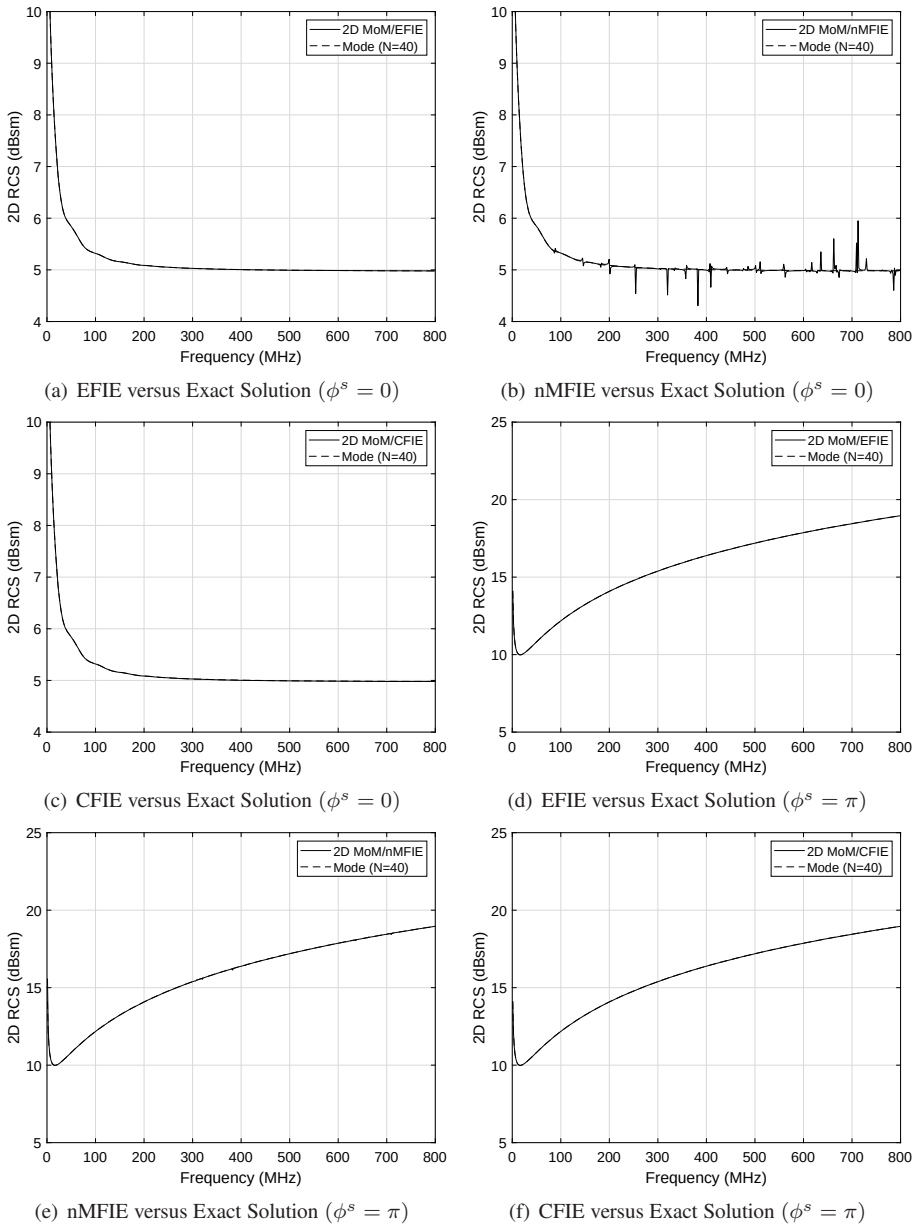
6.1.8.1.2 Results

We first compute the RCS for a conducting cylinder with a radius of 1 meter, for frequencies up to 800 MHz. For the MoM solution, 10 segments per wavelength at 800 MHz were used, yielding 167 segments of equal length. For the modal solution, we terminate the summation at $N = 40$. The backscattering results ($\phi^i = \phi^s = 0$) are summarized in Figures 6.7a–6.7c using the EFIE, nMFIE, and CFIE ($\alpha = 0.5$), respectively. The EFIE does well, at least within the range of frequencies considered, whereas the nMFIE shows many errors due to internal resonances. The CFIE is free of errors, as expected. The RCS in each case is seen to approach the expected high-frequency value of πa, which is approximately 4.97 dBsm in this case. The forward-scattering results ($\phi^i = 0, \phi^s = \pi$) are shown in Figures 6.7d–6.7f. The nMFIE now has less error than in the backscattering case. The RCS in each case tends toward the expected high-frequency value of $4k_0a^2$, which at 800 MHz is approximately 18.26 dBsm.

We next compute the bistatic RCS for $0 \leq \phi^s \leq 2\pi$ and $\phi^i = 0$ at 800 MHz. The CFIE results are compared to the exact solution in Figure 6.8a, where the agreement is excellent. The results obtained using the PO current of (6.100) are shown in Figure 6.8b, where the agreement is good near the specular angles but fair to poor elsewhere.

We then compute the electric current $J_z(\phi^a)$ across all azimuthal angles, for $\phi^i = 0$ at 800 MHz. The real and imaginary components of the currents obtained via the CFIE and PO are compared to the exact solution (6.99) in Figures 6.9a–6.9d, and the amplitudes are compared in Figures 6.9e and 6.9f. The agreement between the modal solution and the CFIE is excellent. The PO current compares fairly well in the illuminated region, however in the shadow region ($\pi/2 \leq \phi^a \leq 3\pi/2$) the PO current is zero.

Finally, we compute the scattered near field in a 10×10 meter region around the cylinder at 800 MHz for $\phi^i = 0$. The normalized real component of the electric field (in V/m) obtained using the CFIE is shown in Figure 6.10a. The modal solution is identical to the eye and is not shown. The fields obtained using PO is shown in Figure 6.10b.



(a) EFIE versus Exact Solution ($\phi^s = 0$)

(b) nMFIE versus Exact Solution ($\phi^s = 0$)

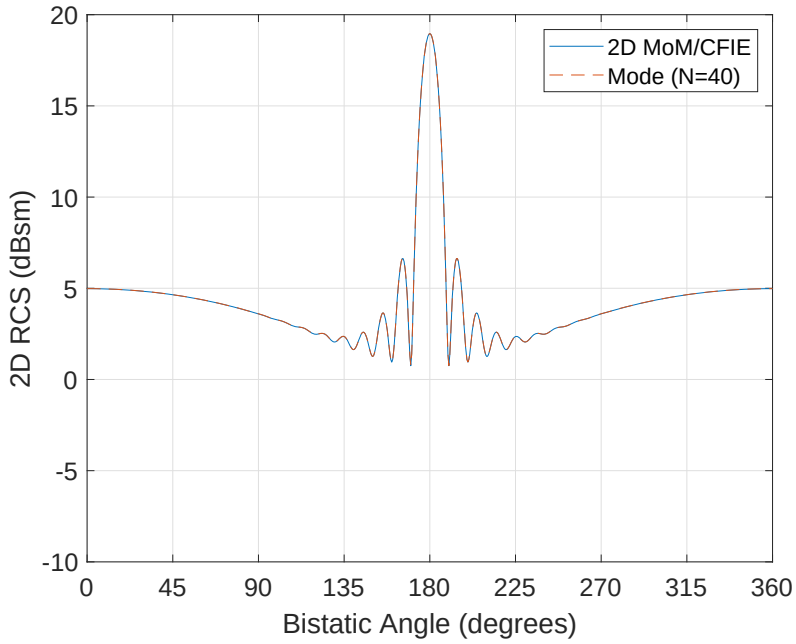
(c) CFIE versus Exact Solution ($\phi^s = 0$)

(d) EFIE versus Exact Solution ($\phi^s = \pi$)

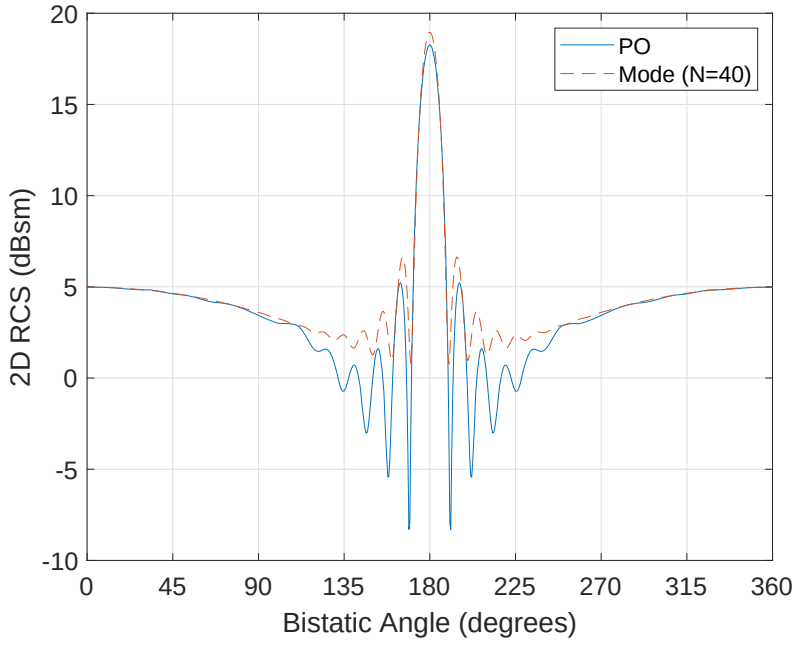
(e) nMFIE versus Exact Solution ($\phi^s = \pi$)

(f) CFIE versus Exact Solution ($\phi^s = \pi$)

Figure 6.7: 2D PEC Cylinder RCS versus Frequency: TM Polarization

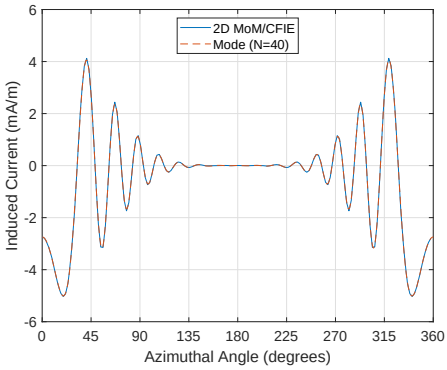


(a) CFIE versus Exact Solution

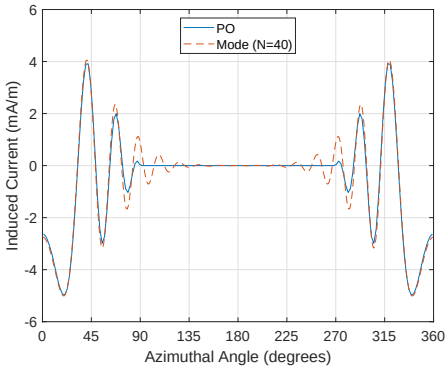


(b) PO versus Exact Solution

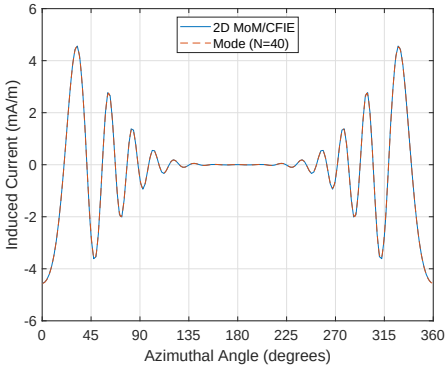
Figure 6.8: 2D PEC Cylinder Bistatic RCS at 800 MHz: TM Polarization



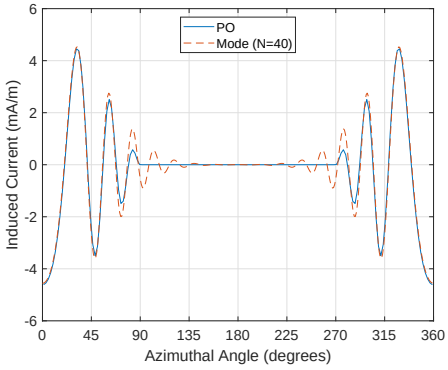
(a) $\mathrm{Re}(J_z(\phi^a))$: CFIE versus Exact Solution



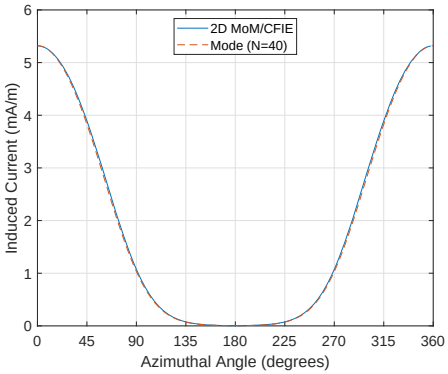
(b) $\mathrm{Re}(J_z(\phi^a))$: PO versus Exact Solution



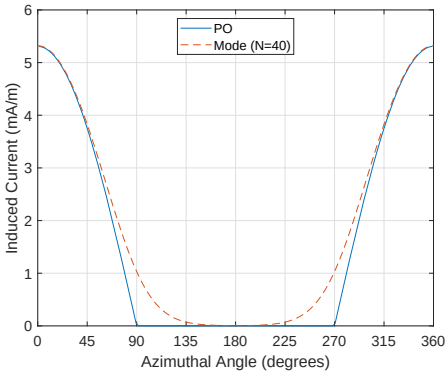
(c) $\mathrm{Im}(J_z(\phi^a))$: CFIE versus Exact Solution



(d) $\mathrm{Im}(J_z(\phi^a))$: PO versus Exact Solution

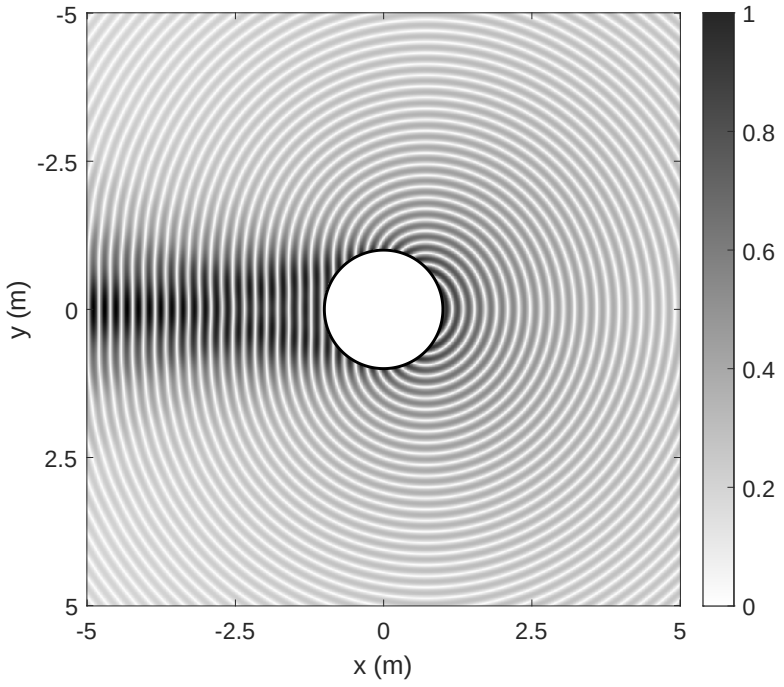


(e) $|J_z(\phi^a)|$: CFIE versus Exact Solution

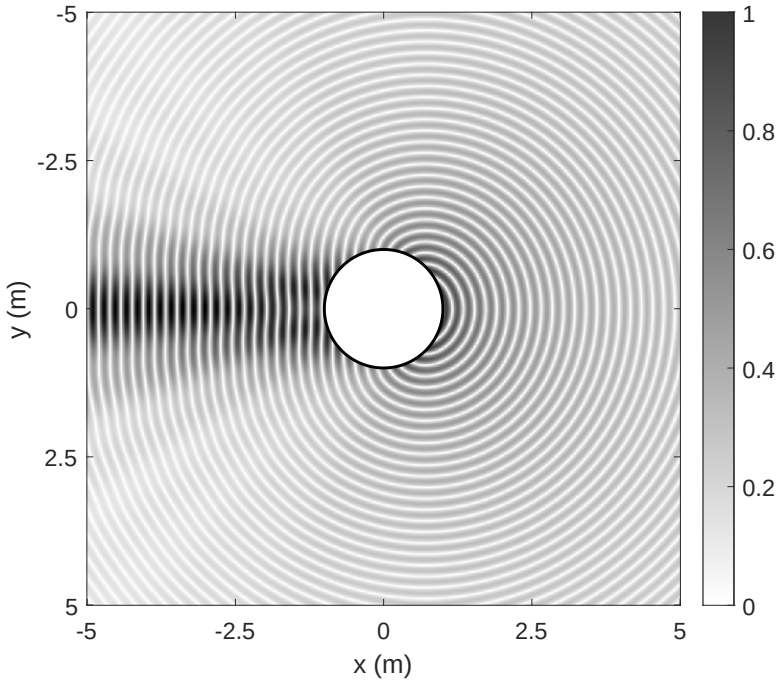


(f) $|J_z(\phi^a)|$: PO versus Exact Solution

Figure 6.9: 2D PEC Cylinder Current versus Azimuthal Angle: TM Polarization



(a) CFIE ($|\operatorname{Re}(\mathbf{E})|$, V/m) at $\phi^i = 0$



(b) PO ($|\operatorname{Re}(\mathbf{E})|$, V/m) at $\phi^i = 0$

Figure 6.10: 2D PEC Cylinder Scattered Near Field at 800 MHz: TM Polarization

6.1.8.2 Conducting Cylinder: TE Polarization

For TE polarization, with a $\hat{\mathbf{z}}$-directed incident magnetic field, the exact solution for the scattered magnetic field is [3] (4.1-3)

$$H_z^s(\rho,\phi^s) = \frac{1}{\eta_0}\sum_{n=0}^{\infty} j^n c_n B_n H_n^{(2)}(k_0\rho)\cos(n\phi^s)\ , \tag{6.102}$$

where $|E_\phi^i| = 1$ for convenience. For the conducting cylinder, the coefficients B_n are [3] (4.1-14)

$$B_n = -\frac{J_n'(k_0 a)}{H_n'^{(2)}(k_0 a)}\ . \tag{6.103}$$

The scattered far magnetic field is [3] (4.1-6)

$$H_z^s(\rho,\phi^s) = \frac{1}{\eta_0}\sqrt{\frac{2}{\pi}}\frac{e^{-j(k_0\rho-\pi/4)}}{\sqrt{k_0\rho}}\sum_{n=0}^{\infty}(-1)^n c_n B_n\cos n\phi^s\ . \tag{6.104}$$

The induced azimuthal electric current $J_z(\phi^a)$ is [3] (4.1-15)

$$\mathbf{J}(\phi^a) = \frac{2j}{\eta_0\pi k_0 a}\sum_{n=0}^{\infty}\frac{j^n c_n\cos n\phi^a}{H_n'^{(2)}(k_0 a)}\hat{\boldsymbol{\phi}}\ , \tag{6.105}$$

where ϕ^a is the azimuthal angle on the surface of the cylinder. The recurrence relationship [2]

$$Z_n'(ka) = \frac{n}{ka}Z_n(ka) - Z_{n+1}(ka) \tag{6.106}$$

can be used to compute the derivatives, where Z_n represents either J_n or H_n.

Noting that on the cylinder, $\hat{\mathbf{n}} = \hat{\boldsymbol{\rho}}$, for angles ϕ^a in the illuminated region the PO current (6.89) is then

$$\mathbf{J}_\phi^{\mathrm{PO}}(\phi^a) = -\frac{2}{\eta}e^{jk(x\cos\phi^i + y\sin\phi^i)}\hat{\boldsymbol{\phi}}\ , \tag{6.107}$$

and in the shadowed region, $\mathbf{J}_\phi^{PO}(\phi^a) = 0$.

6.1.8.2.1 MoM Linear System

For the TE case, the MoM linear system is obtained from (6.101) by simply interchanging the z and t superscripts.

6.1.8.2.2 Results

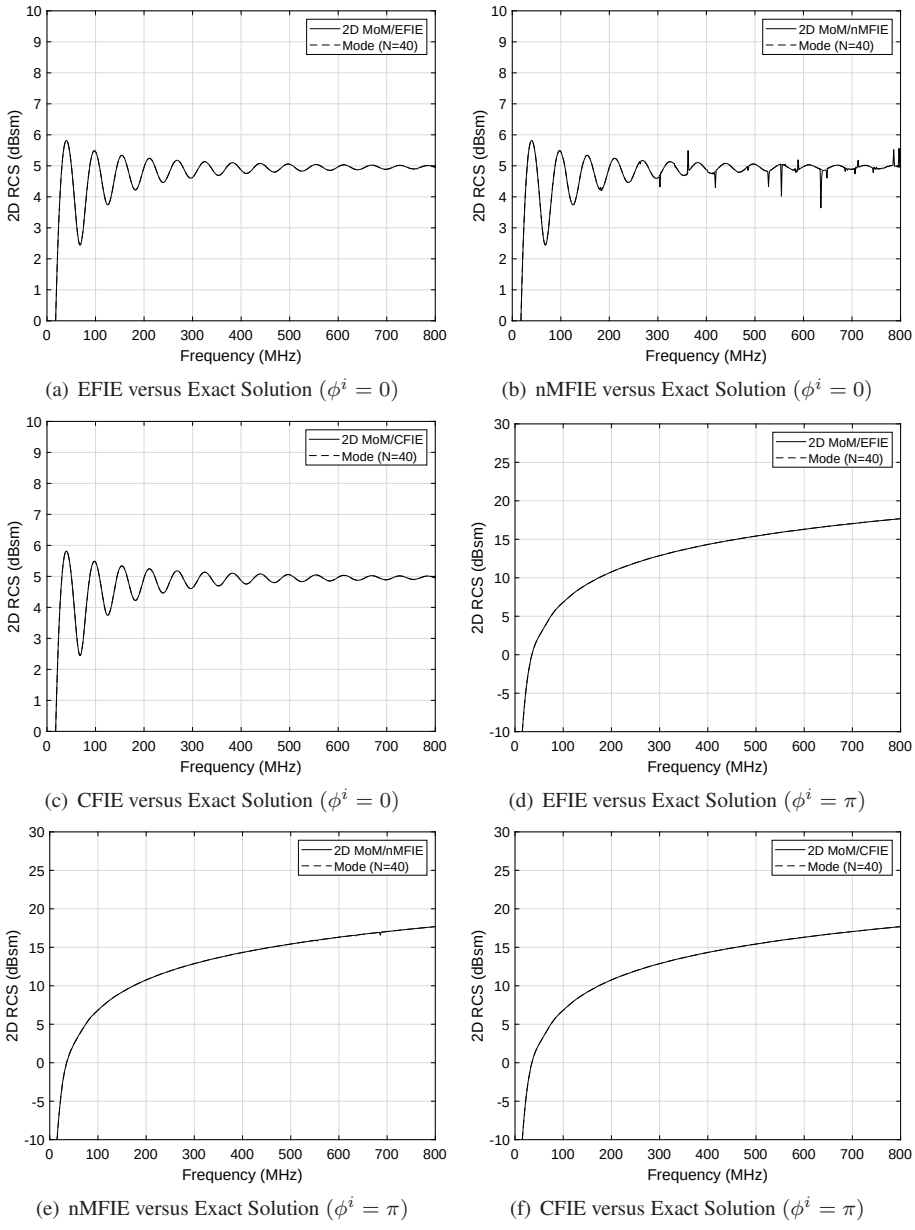
For TE polarization, we use the same conducting cylinder and numerical parameters as in the TM case. The backscatter results are summarized in Figures 6.11a–6.11c using EFIE, nMFIE, and CFIE, respectively. The nMFIE again shows errors due to internal resonances, and the CFIE is free of errors, as expected. The RCS in each case

again approaches the high-frequency limit of approximately 4.97 dBsm. The forward-scattering results are shown in Figures 6.11d–6.11f. The nMFIE again shows some errors but they are again not as apparent as in the backscattering direction. The RCS in each case approaches the expected high-frequency limit of approximately 18.26 dBsm at 800 MHz.

We next compute the bistatic RCS for $0 \leq \phi^s \leq 2\pi$ and $\phi^i = 0$ at 800 MHz. The CFIE results are compared to the exact solution in Figure 6.12a, and the agreement is again excellent. The results obtained using the PO current of (6.107) are shown in Figure 6.12b. The agreement is fair near the specular angles, but poor elsewhere.

We next compute the electric current $J_\phi(\phi^a)$ across all azimuthal angles for $\phi^i = 0$ at 800 MHz. The real and imaginary components of the currents obtained via CFIE and PO are compared to the exact solution (6.99) in Figures 6.13a–6.13d, and the amplitudes compared in Figures 6.13e and 6.13f. The agreement between the modal solution and the CFIE is fairly good, however he PO current does not agree very well at all, as its amplitude comprises a step function in the TE case. This inaccuracy is a likely source of the disagreement in the bistatic RCS seen previously in Figure 6.12b.

Finally, we compute the scattered near field in a 10×10 meter region about the cylinder at 800 MHz for $\phi^i = 0$. The normalized amplitude of the real part of the electric field (in V/m) obtained using the CFIE is shown in Figure 6.14a. The modal solution is identical to the eye and is not shown. The corresponding solution obtained using Physical Optics is shown in Figure 6.14b.



(a) EFIE versus Exact Solution ($\phi^i = 0$)

(b) nMFIE versus Exact Solution ($\phi^i = 0$)

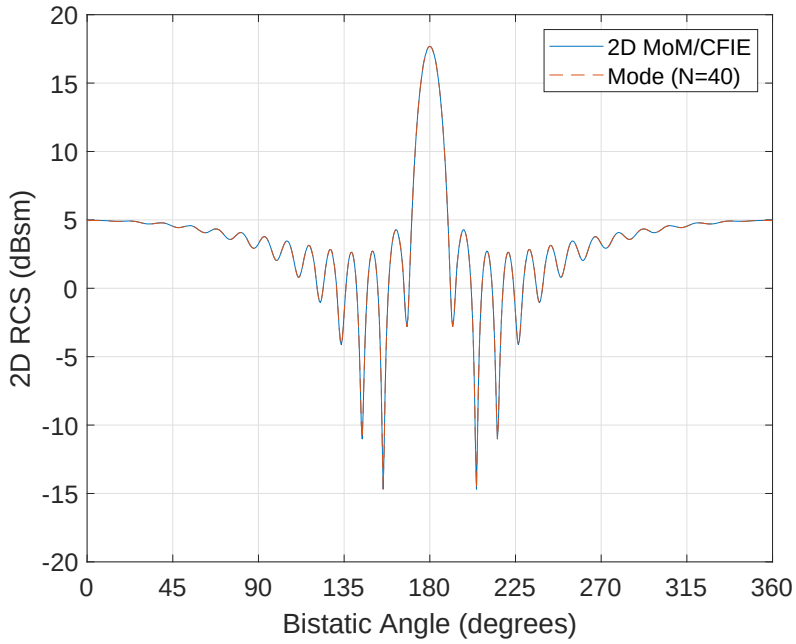
(c) CFIE versus Exact Solution ($\phi^i = 0$)

(d) EFIE versus Exact Solution ($\phi^i = \pi$)

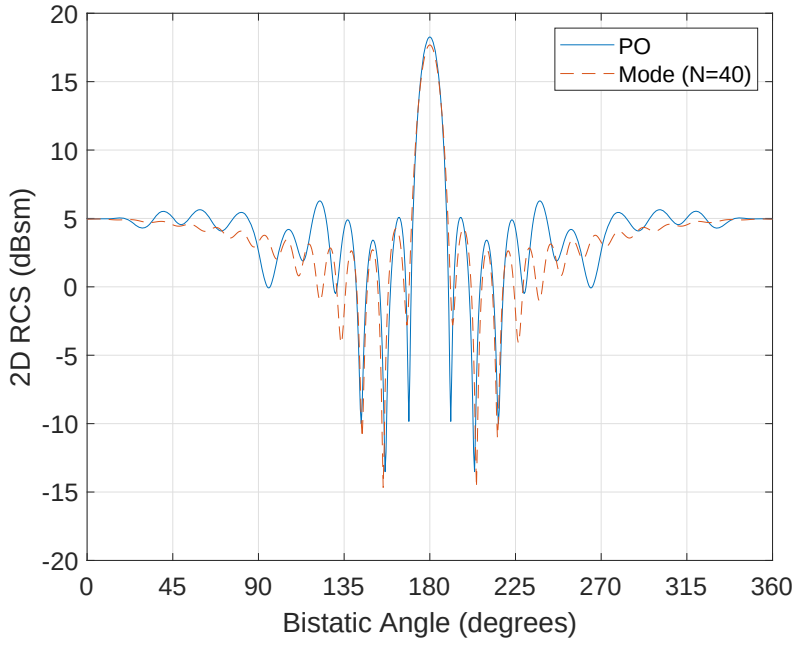
(e) nMFIE versus Exact Solution ($\phi^i = \pi$)

(f) CFIE versus Exact Solution ($\phi^i = \pi$)

Figure 6.11: 2D PEC Cylinder RCS versus Frequency: TE Polarization

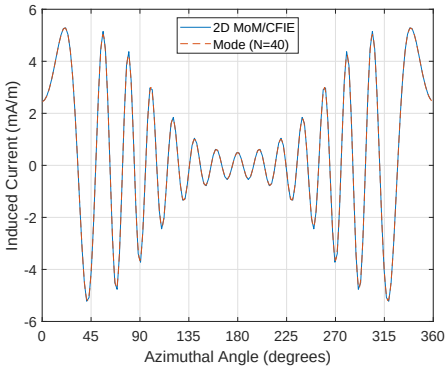


(a) CFIE versus Exact Solution

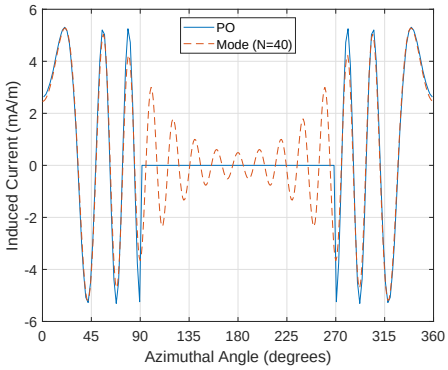


(b) PO versus Exact Solution

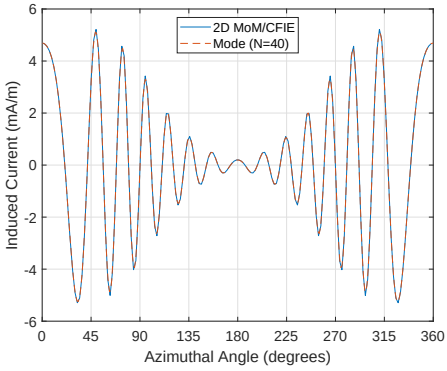
Figure 6.12: 2D PEC Cylinder Bistatic RCS at 800 MHz: TE Polarization



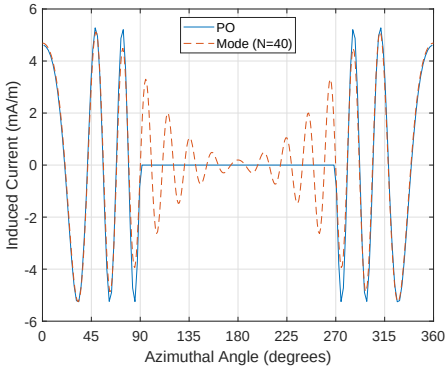
(a) $\mathrm{Re}(J_\phi(\phi^a))$: CFIE versus Exact Solution



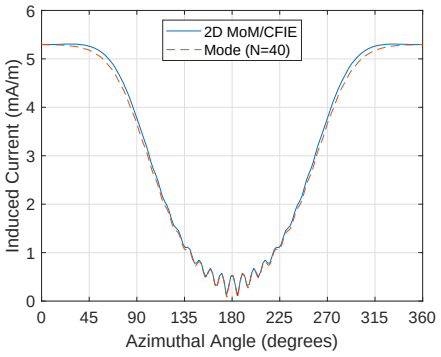
(b) $\mathrm{Re}(J_\phi(\phi^a))$: PO versus Exact Solution



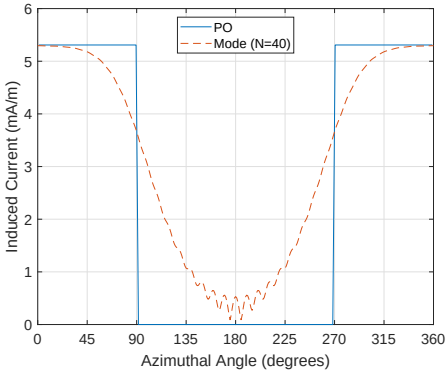
(c) $\mathrm{Im}(J_\phi(\phi^a))$: CFIE versus Exact Solution



(d) $\mathrm{Im}(J_\phi(\phi^a))$: PO versus Exact Solution

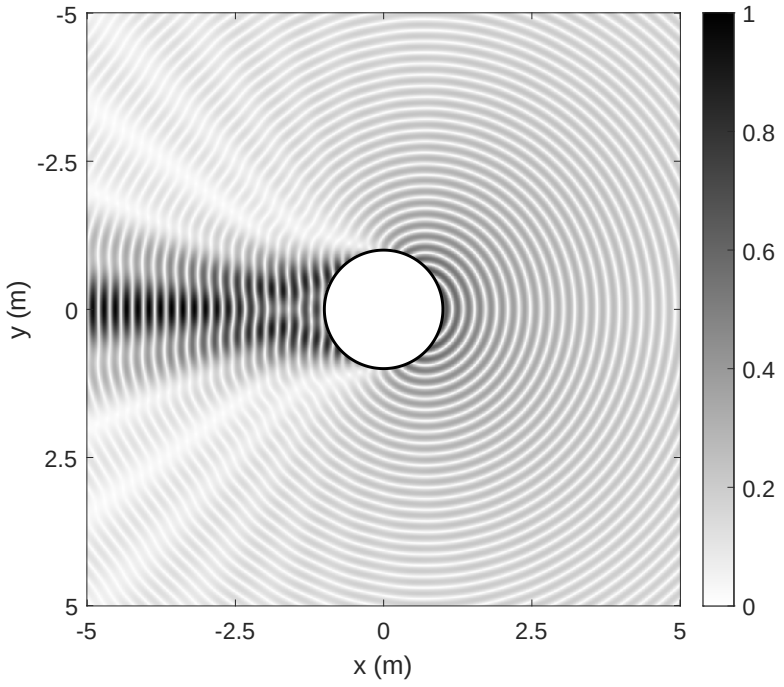


(e) $|J_\phi(\phi^a)|$: CFIE versus Exact Solution

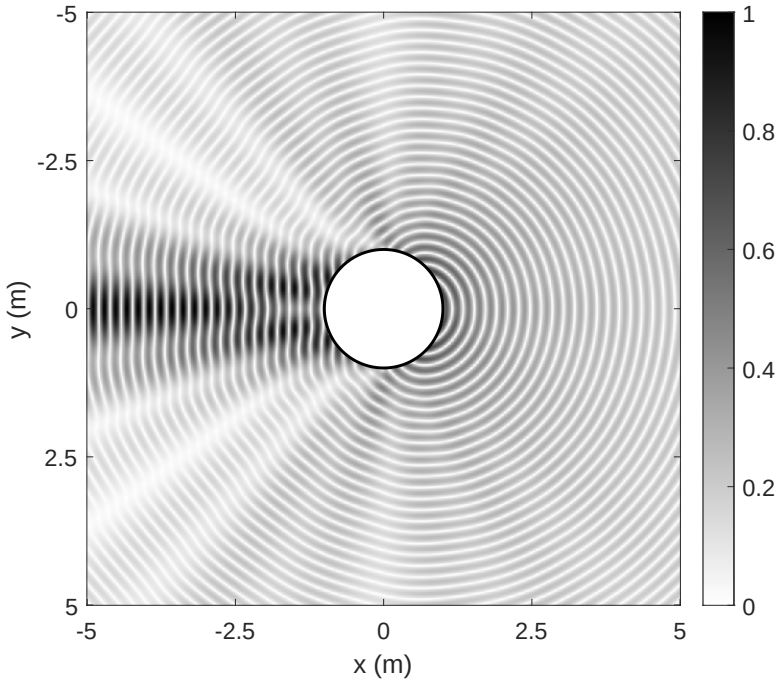


(f) $|J_\phi(\phi^a)|$: PO versus Exact Solution

Figure 6.13: 2D PEC Cylinder Current versus Azimuthal Angle: TE Polarization



(a) CFIE ($|\operatorname{Re}(\mathbf{E})|$, V/m) at $\phi^i = 0$



(b) PO ($|\operatorname{Re}(\mathbf{E})|$, V/m) at $\phi^i = 0$

Figure 6.14: 2D PEC Cylinder Scattered Near Field at 800 MHz: TE Polarization

6.2 Dielectric and Composite Objects

In this section, we build upon the work from Section 6.1 to create a framework for treating two-dimensional dielectric and composite dielectric/conducting objects (without junctions). We will use the expressions previously derived for the EFIE and nMFIE that involved the $\mathcal{L}$ and $\hat{\mathbf{n}} \times \mathcal{K}$ operators, and develop new expressions involving the $\mathcal{K}$ and $\hat{\mathbf{n}} \times \mathcal{L}$ operators. As before, we will consider each integral equation in TM and TE polarization separately, and we will present generalized MoM discretizations exclusively in terms of triangle basis and testing functions. We will then present several examples.

6.2.1 Basis Function Orientation

As we begin to study multi-region problems in more detail, the orientation of the basis functions on the various dielectric interfaces must be considered carefully. As there are $\hat{\mathbf{z}}$-directed electric currents and tangentially directed magnetic currents in the TM case, and vice versa for the TE case, we will treat the orientations of both currents in a self-consistent manner. Consider a triangle function having support on segments $s+$ and $s-$, whose endpoints comprise $(\mathbf{p}_{k-1}, \mathbf{p}_k, \mathbf{p}_{k+1})$. The segments reside on the interface S_{12} between dielectric regions R_1 and R_2, as shown in Figure 6.15. First, we define the unit vectors

$$\hat{\mathbf{t}}^{s+} = \frac{\mathbf{p}_{k+1} - \mathbf{p}_k}{|\mathbf{p}_{k+1} - \mathbf{p}_k|} \tag{6.108}$$

and

$$\hat{\mathbf{t}}^{s-} = \frac{\mathbf{p}_k - \mathbf{p}_{k-1}}{|\mathbf{p}_k - \mathbf{p}_{k-1}|} \,. \tag{6.109}$$

We know from Section 3.6.3 that the currents on each side of the interface must flow in opposite directions. Therefore, let us define R_1 as the "positive" side of the interface. On the positive side, the vectors normal to each segment are

$$\hat{\mathbf{n}}_1^{s+} = \hat{\mathbf{t}}^{s+} \times \hat{\mathbf{z}} \tag{6.110}$$

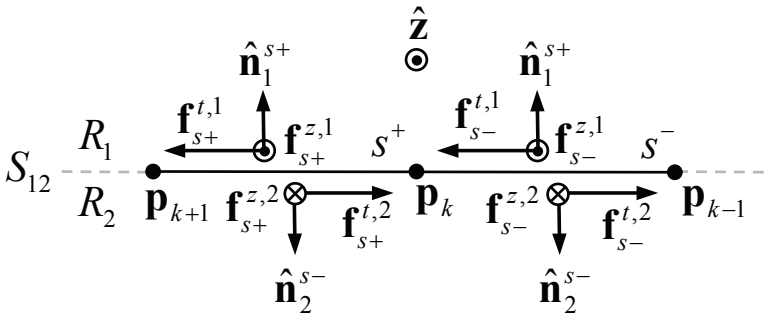


Figure 6.15: Basis Function Orientation for 2D Problems

and

$$\hat{\mathbf{n}}_1^{s-} = \hat{\mathbf{t}}^{s-} \times \hat{\mathbf{z}} \, . \tag{6.111}$$

As we are still free to orient the basis functions, we begin in R_1, and make the following assignments for the tangential basis function:

$$\hat{\mathbf{f}}_{s+}^{t,1} = \hat{\mathbf{t}}^{s+} \tag{6.112}$$

and

$$\hat{\mathbf{f}}_{s-}^{t,1} = \hat{\mathbf{t}}^{s-} \, . \tag{6.113}$$

and the following assignments for the $\hat{\mathbf{z}}$-oriented basis function:

$$\hat{\mathbf{f}}_{s+}^{z,1} = \hat{\mathbf{z}} \tag{6.114}$$

and

$$\hat{\mathbf{f}}_{s-}^{z,1} = \hat{\mathbf{z}} \, . \tag{6.115}$$

If we now move to the opposite or "negative" side of the interface in R_2, we need only reverse the direction of the normal vector and the basis functions in R_1, as shown in Figure 6.15. We refer to this as a right-handed boundary orientation. Note that all currents have opposite orientations on each side of the interface, and for tangentially oriented currents, Kirchhoff's law is satisfied at p_k. We will use this orientation again when discussing bodies of revolution in Chapter 7.

6.2.2 EFIE: TM Polarization

The EFIE (3.181) for TM polarization has an $\mathcal{L}$ operator acting on the $\hat{\mathbf{z}}$-directed electric current $\mathbf{J}(\boldsymbol{\rho})$, and a $\mathcal{K}$ operator acting on the tangential magnetic current $\mathbf{M}(\boldsymbol{\rho})$. In region R_l, these expressions are

$$\int_C \left[1 + \frac{1}{k_l^2} \nabla\nabla \cdot \right] \mathbf{J}(\boldsymbol{\rho}') H_0^{(2)}\big(k_l |\boldsymbol{\rho} - \boldsymbol{\rho}'|\big) \, d\boldsymbol{\rho}' \, , \tag{6.116}$$

and

$$\frac{1}{2} \hat{\mathbf{n}}_l(\boldsymbol{\rho}) \times \mathbf{M}(\boldsymbol{\rho}) - \frac{jk_l}{4} \int_{C'} \mathbf{M}(\boldsymbol{\rho}') \times \hat{\mathbf{R}}(\boldsymbol{\rho}, \boldsymbol{\rho}') \, H_1^{(2)}(k_l \rho) \, d\boldsymbol{\rho}' \, . \tag{6.117}$$

6.2.2.1 MoM Discretization

Testing (6.116) and (6.117) with the $\hat{\mathbf{z}}$-oriented electric basis functions yields the matrix elements (3.188) and (3.189) for the TM case, which are

$$Z_{mn}^{EJ(l),TM} = \frac{\omega \mu_l}{4} \mathrm{L}^{zz}(\mathbf{f}_m^z, \mathbf{f}_n^z) \tag{6.118}$$

and

$$Z_{mn}^{EM(l),TM} = \mathrm{K}^{zt}(\mathbf{f}_m^z, \mathbf{g}_n^t) \, . \tag{6.119}$$

The function L^{zz} was summarized in (6.25). The function K^{zt} is

$$\mathrm{K}^{zt}(\mathbf{f}_m^z, \mathbf{g}_n^t) = \frac{1}{2}\int_{\mathbf{f}_m^z=\mathbf{g}_n^t} \mathbf{f}_m^z(\boldsymbol{\rho}) \cdot \Big[\hat{\mathbf{n}}_l(\boldsymbol{\rho}) \times \mathbf{g}_n^t(\boldsymbol{\rho})\Big]\, d\boldsymbol{\rho} \\ -\frac{jk_l}{4}\int_{\mathbf{f}_m^z} \mathbf{f}_m^z(\boldsymbol{\rho}) \cdot \int_{\mathbf{g}_n^t} \mathbf{g}_n^t(\boldsymbol{\rho}') \times \hat{\mathbf{R}}(\boldsymbol{\rho}, \boldsymbol{\rho}')\, H_1^{(2)}(k_l\rho)\, d\boldsymbol{\rho}'\, d\boldsymbol{\rho}\,. \quad (6.120)$$

where the first term is evaluated over boundary segments where $\mathbf{f}_m^z$ and $\mathbf{g}_n^t$ overlap, and the second where they do not. The EFIE right-hand side vector elements (3.194) for TM polarization are

$$V_m^{z,E} = \int_{\mathbf{f}_m^z} \mathbf{f}_m^z(\boldsymbol{\rho}) \cdot \mathbf{E}_z^i(\boldsymbol{\rho})\, d\boldsymbol{\rho}\,. \quad (6.121)$$

6.2.3 MFIE: TM Polarization

The MFIE (3.182) for TM-polarization has an $\mathcal{L}$ operator acting on the tangential magnetic current $\mathbf{M}(\boldsymbol{\rho})$, and a $\mathcal{K}$ operator acting on the $\hat{\mathbf{z}}$-directed electric current $\mathbf{J}(\boldsymbol{\rho})$. In region R_l, these expressions are

$$\int_C \left[1 + \frac{1}{k_l^2}\nabla\nabla\cdot\right] \mathbf{M}(\boldsymbol{\rho}') H_0^{(2)}\big(k_l|\boldsymbol{\rho}-\boldsymbol{\rho}'|\big)\, d\boldsymbol{\rho}' \quad (6.122)$$

and

$$-\frac{1}{2}\hat{\mathbf{n}}_l(\boldsymbol{\rho}) \times \mathbf{J}(\boldsymbol{\rho}) + \frac{jk_l}{4}\int_{C'} \mathbf{J}(\boldsymbol{\rho}') \times \hat{\mathbf{R}}(\boldsymbol{\rho}, \boldsymbol{\rho}')\, H_1^{(2)}(k_l\rho)\, d\boldsymbol{\rho}'\,. \quad (6.123)$$

6.2.3.1 MoM Discretization

Testing (6.122) and (6.123) with the tangential magnetic basis functions yields the matrix elements (3.190) and (3.191), which are

$$Z_{mn}^{HM(l),TM} = \frac{\omega\epsilon_l}{4}\mathrm{L}^{tt}(\mathbf{g}_m^t, \mathbf{g}_n^t) \quad (6.124)$$

and

$$Z_{mn}^{HJ(l),TM} = -\mathrm{K}^{tz}(\mathbf{g}_m^t, \mathbf{f}_n^z)\,. \quad (6.125)$$

The function L^{tt} was summarized in (6.69). The function K^{tz} is identical to (6.120) except that t and z are interchanged. Therefore, it can be written as

$$\mathrm{K}^{tz}(\mathbf{g}_m^t, \mathbf{f}_n^z) = \frac{1}{2}\int_{\mathbf{g}_m^t=\mathbf{f}_n^z} \mathbf{g}_m^t(\boldsymbol{\rho}) \cdot \Big[\hat{\mathbf{n}}_l(\boldsymbol{\rho}) \times \mathbf{f}_n^z(\boldsymbol{\rho})\Big]\, d\boldsymbol{\rho} \\ -\frac{jk_l}{4}\int_{\mathbf{g}_m^t} \mathbf{g}_m^t(\boldsymbol{\rho}) \cdot \int_{\mathbf{f}_n^z} \mathbf{f}_n^z(\boldsymbol{\rho}') \times \hat{\mathbf{R}}(\boldsymbol{\rho}, \boldsymbol{\rho}')\, H_1^{(2)}(k_l\rho)\, d\boldsymbol{\rho}'\, d\boldsymbol{\rho}\,. \quad (6.126)$$

The MFIE right-hand side vector elements (3.195) for TM polarization are

$$V_m^{t,E} = \int_{\mathbf{g}_m^t} \mathbf{g}_m^t(\boldsymbol{\rho}) \cdot \mathbf{H}_t^i(\boldsymbol{\rho})\, d\boldsymbol{\rho}\,. \quad (6.127)$$

6.2.4 nMFIE: TM Polarization

The nMFIE (3.183) for TM polarization has an $\hat{\mathbf{n}} \times \mathcal{L}$ operator acting on the tangential magnetic current $\mathbf{M}(\boldsymbol{\rho})$, and an $\hat{\mathbf{n}} \times \mathcal{K}$ operator acting on the $\hat{\mathbf{z}}$-directed electric current $\mathbf{J}(\boldsymbol{\rho})$. In region R_l, these expressions are

$$\frac{1}{2}\mathbf{J}(\boldsymbol{\rho}) + \frac{jk_l}{4}\hat{\mathbf{n}}(\boldsymbol{\rho}) \times \int_{C'} \mathbf{J}(\boldsymbol{\rho}') \times \hat{\mathbf{R}}(\boldsymbol{\rho}, \boldsymbol{\rho}')\, H_1^{(2)}(k_l\rho)\, d\boldsymbol{\rho}' \tag{6.128}$$

and

$$\hat{\mathbf{n}}_l(\boldsymbol{\rho}) \times \int_C \left[1 + \frac{1}{k_l^2}\nabla\nabla\cdot\right] \mathbf{M}(\boldsymbol{\rho}') H_0^{(2)}\big(k_l|\boldsymbol{\rho} - \boldsymbol{\rho}'|\big)\, d\boldsymbol{\rho}' \,. \tag{6.129}$$

6.2.4.1 MoM Discretization

Testing (6.128) and (6.129) with the $\hat{\mathbf{z}}$-oriented electric basis functions yields the matrix elements (3.192) and (3.193) for the TM case, which are

$$Z_{mn}^{nHJ(l),TM} = \mathrm{nK}^{zz}(\mathbf{f}_m^z, \mathbf{f}_n^z) \tag{6.130}$$

and

$$Z_{mn}^{nHM(l),TM} = \frac{\omega\epsilon_l}{4}\mathrm{nL}^{zt}(\mathbf{f}_m^z, \mathbf{g}_n^t) \,. \tag{6.131}$$

The function nK^{zz} was summarized in (6.80). The function nL^{zt} is

$$\begin{aligned}\mathrm{nL}^{zt}(\mathbf{f}_m^z, \mathbf{g}_n^t) = &\int_{\mathbf{f}_m^z} \mathbf{f}_m^z(\boldsymbol{\rho}) \cdot \hat{\mathbf{n}}_l(\boldsymbol{\rho}) \times \int_{\mathbf{g}_n^t} \mathbf{g}_n^t(\boldsymbol{\rho}')\, H_0^{(2)}\big(k_l|\boldsymbol{\rho} - \boldsymbol{\rho}'|\big)\, d\boldsymbol{\rho}'\, d\boldsymbol{\rho} \\ -\frac{1}{k_l^2}&\int_{\mathbf{f}_m^z} \nabla\cdot\Big[\mathbf{f}_m^z(\boldsymbol{\rho}) \times \hat{\mathbf{n}}_l(\boldsymbol{\rho})\Big] \int_{\mathbf{g}_n^t} \nabla'\cdot\mathbf{g}_n^t(\boldsymbol{\rho}')\, H_0^{(2)}\big(k_l|\boldsymbol{\rho} - \boldsymbol{\rho}'|\big)\, d\boldsymbol{\rho}'\, d\boldsymbol{\rho} \,.\end{aligned} \tag{6.132}$$

where we have used (3.208). Note that the term $\mathbf{f}_m^z(\boldsymbol{\rho}) \times \hat{\mathbf{n}}_l(\boldsymbol{\rho})$ results in a tangentially oriented vector on each segment, thus, the second term in (6.132) is evaluated in a similar way as the one in (6.69). The nMFIE right-hand side vector elements (3.196) for TM polarization are

$$V_m^{z,nH} = \int_{\mathbf{f}_m^z} \mathbf{f}_m^z(\boldsymbol{\rho}) \cdot \big[\hat{\mathbf{n}}_l(\boldsymbol{\rho}) \times \mathbf{H}_t^i(\boldsymbol{\rho})\big]\, d\boldsymbol{\rho} \,. \tag{6.133}$$

6.2.5 EFIE: TE Polarization

The operators in the EFIE for TE polarization are the dual of those from the MFIE in the TM case, where the electric and magnetic currents are exchanged. Therefore, we will simply summarize the MoM discretization.

6.2.5.1 MoM Discretization

The matrix elements (3.188) and (3.189) for the TE case are

$$Z_{mn}^{EJ(l),TE} = \frac{\omega\mu_l}{4}\mathrm{L}^{tt}(\mathbf{f}_m^t, \mathbf{f}_n^t) \tag{6.134}$$

and

$$Z_{mn}^{EM(l),TE} = \mathrm{K}^{tz}(\mathbf{f}_m^t, \mathbf{g}_n^z)\ . \tag{6.135}$$

The EFIE right-hand side vector elements (3.194) for the TE case are

$$V_m^{t,E} = \int_{\mathbf{f}_m^t} \mathbf{f}_m^t(\boldsymbol{\rho}) \cdot \mathbf{E}_t^i(\boldsymbol{\rho})\ d\boldsymbol{\rho}\ . \tag{6.136}$$

6.2.6 MFIE: TE Polarization

Similarly, the operators in the MFIE for TE polarization are the dual of those from the EFIE in the TM case, with the electric and magnetic currents exchanged. Thus, we will simply summarize the MoM discretization.

6.2.6.1 MoM Discretization

The matrix elements (3.190) and (3.191) for the TE case are

$$Z_{mn}^{HM(l),TE} = \frac{\omega\epsilon_l}{4}\mathrm{L}^{zz}(\mathbf{g}_m^z, \mathbf{g}_n^z) \tag{6.137}$$

and

$$Z_{mn}^{HJ(l),TE} = -\mathrm{K}^{zt}(\mathbf{g}_m^z, \mathbf{f}_n^t)\ . \tag{6.138}$$

The MFIE right-hand side vector elements (3.195) for the TE case are

$$V_m^{z,H} = \int_{\mathbf{g}_m^z} \mathbf{g}_m^z(\boldsymbol{\rho}) \cdot \mathbf{H}_z^i(\boldsymbol{\rho})\ d\boldsymbol{\rho}\ . \tag{6.139}$$

6.2.7 nMFIE: TE Polarization

The expressions for the nMFIE for TE-polarization are functionally identical to those of the nMFIE for TM-polarization, except that t and z are interchanged. Thus, we will simply summarize the MoM discretization.

6.2.7.1 MoM Discretization

The matrix elements (3.192) and (3.193) for the TE case are

$$Z_{mn}^{nHJ(l),TE} = \mathrm{nK}^{tt}(\mathbf{f}_m^t, \mathbf{f}_n^t) \tag{6.140}$$

and

$$Z_{mn}^{nHM(l),TE} = \frac{\omega\epsilon_l}{4}\mathrm{nL}^{tz}(\mathbf{f}_m^t, \mathbf{g}_n^z)\ . \tag{6.141}$$

The function nK^{tt} was summarized in (6.91). The function nL^{tz} is

$$\mathrm{nL}^{tz}(\mathbf{f}_m^t, \mathbf{g}_n^z) = \int_{\mathbf{f}_m^t} \mathbf{f}_m^t(\boldsymbol{\rho}) \cdot \int_{\mathbf{g}_n^z} \hat{\mathbf{n}}_l(\boldsymbol{\rho}) \times \mathbf{g}_n^z(\boldsymbol{\rho}')\, H_0^{(2)}\big(k_l|\boldsymbol{\rho} - \boldsymbol{\rho}'|\big)\, d\boldsymbol{\rho}'\, d\boldsymbol{\rho}\,, \tag{6.142}$$

where the second term on the right in (6.132) goes to zero, since

$$\nabla \cdot \Big[\mathbf{f}_m^t(\boldsymbol{\rho}) \times \hat{\mathbf{n}}_l(\boldsymbol{\rho})\Big] = 0\,. \tag{6.143}$$

The nMFIE right-hand side vector elements (3.196) for the TE case are

$$V_m^{t,nH} = \int_{\mathbf{f}_t^z} \mathbf{f}_m^t(\boldsymbol{\rho}) \cdot \big[\hat{\mathbf{n}}_l(\boldsymbol{\rho}) \times \mathbf{H}_z^i(\boldsymbol{\rho})\big]\; d\boldsymbol{\rho}\,. \tag{6.144}$$

6.2.8 Numerical Stability

Consider an MoM system matrix that has been constructed from the EFIE and MFIE. In very general terms, it can be represented via the block structure

$$Z = \begin{bmatrix} \mathrm{L}(\mathbf{f},\mathbf{f}) & \mathrm{K}(\mathbf{f},\mathbf{g}) \\ -\mathrm{K}(\mathbf{g},\mathbf{f}) & \frac{\epsilon}{\mu}\mathrm{L}(\mathbf{g},\mathbf{g}) \end{bmatrix}. \tag{6.145}$$

Note that the matrix block in the lower right is scaled down by $1/\eta^2$ versus the block in the upper left. This disparity in amplitude tends to cause numerical stability issues in the linear system, due to limitations in the floating point representation. As a remedy, we will use the approach from [4], where the magnetic basis function is everywhere scaled by η_0. That is,

$$\mathbf{g}^{t,z} = \eta_0 \mathbf{f}^{t,z}. \tag{6.146}$$

This modification works very well in practice, and we incorporate this scale factor into all the magnetic basis functions throughout the remainder of this book.

6.2.9 Examples

In this section we apply the expressions developed in this section to the scattering of plane waves by a homogeneous dielectric cylinder and a coated, conducting cylinder. Lossless and lossy dielectrics are considered.

6.2.9.1 Dielectric Cylinder

Consider a homogeneous dielectric circular cylinder of radius a with dielectric parameters (ϵ_1, μ_1). We divide the problem into an interior region R_1 with the aforementioned parameters, and the external free space region R_0 with material parameters (ϵ_0, μ_0), which are separated by the interface S_{01}. Using the PMCHWT approach, we compute the EFIE and MFIE on S_{01} in both R_0 and R_1. We then sum the resulting EFIEs and MFIEs on each side of the interface by combining the columns and rows for the basis and testing functions on S_{01}.

6.2.9.1.1 Dielectric Cylinder: TM Polarization

For the exact modal solution of a dielectric cylinder, the series coefficients A_n for TM polarization are [3]

$$A_n = -\frac{(k_1/\mu_1)J_n(k_0a)J_n'(k_1a) - (k_0/\mu_0)J_n'(k_0a)J_n(k_1a)}{(k_1/\mu_1)H_n^{(2)}(k_0a)J_n'(k_1a) - (k_0/\mu_0)H_n'^{(2)}(k_0a)J_n(k_1a)}\,, \tag{6.147}$$

where the scattered field is given by (6.96).

6.2.9.1.2 MoM Linear System

For the TM case, the MoM linear system can be written as

$$\begin{bmatrix} Z^{zz} & Z^{zt} \\ Z^{tz} & Z^{tt} \end{bmatrix} \begin{bmatrix} J^z_{S_{01}} \\ M^t_{S_{01}} \end{bmatrix} = \begin{bmatrix} V^{E,z} \\ V^{H,t} \end{bmatrix}, \tag{6.148}$$

where the blocks of the MoM system matrix are

$$Z^{zz} = \frac{\omega\mu_0}{4}\mathrm{L}^{zz}\big(\mathbf{f}^z_{S_{01}}, \mathbf{f}^z_{S_{01}}, R_0\big) + \frac{\omega\mu_1}{4}\mathrm{L}^{zz}\big(\mathbf{f}^z_{S_{01}}, \mathbf{f}^z_{S_{01}}, R_1\big)\,, \tag{6.149}$$

$$Z^{zt} = \mathrm{K}^{zt}\big(\mathbf{f}^z_{S_{01}}, \mathbf{g}^t_{S_{01}}, R_0\big) + \mathrm{K}^{zt}\big(\mathbf{f}^z_{S_{01}}, \mathbf{g}^t_{S_{01}}, R_1\big)\,, \tag{6.150}$$

$$Z^{tz} = -\mathrm{K}^{tz}\big(\mathbf{g}^t_{S_{01}}, \mathbf{f}^z_{S_{01}}, R_0\big) - \mathrm{K}^{tz}\big(\mathbf{g}^t_{S_{01}}, \mathbf{f}^z_{S_{01}}, R_1\big)\,, \tag{6.151}$$

$$Z^{tt} = \frac{\omega\epsilon_0}{4}\mathrm{L}^{tt}\big(\mathbf{g}^t_{S_{01}}, \mathbf{g}^t_{S_{01}}, R_0\big) + \frac{\omega\epsilon_1}{4}\mathrm{L}^{tt}\big(\mathbf{g}^t_{S_{01}}, \mathbf{g}^t_{S_{01}}, R_1\big)\,. \tag{6.152}$$

The notation $\mathrm{X}\big(\mathbf{a}_{S_{mn}}, \mathbf{b}_{S_{pq}}, R_l\big)$ indicates that X is evaluated in R_l for the testing and basis functions **a** and **b** that reside on the boundaries S_{mn} and S_{pq}, respectively, using the appropriate vector orientations in that region. The right-hand side vectors are

$$V^{E,z} = V^E\big(\mathbf{f}^z_{S_{01}}, R_0\big) \tag{6.153}$$

and

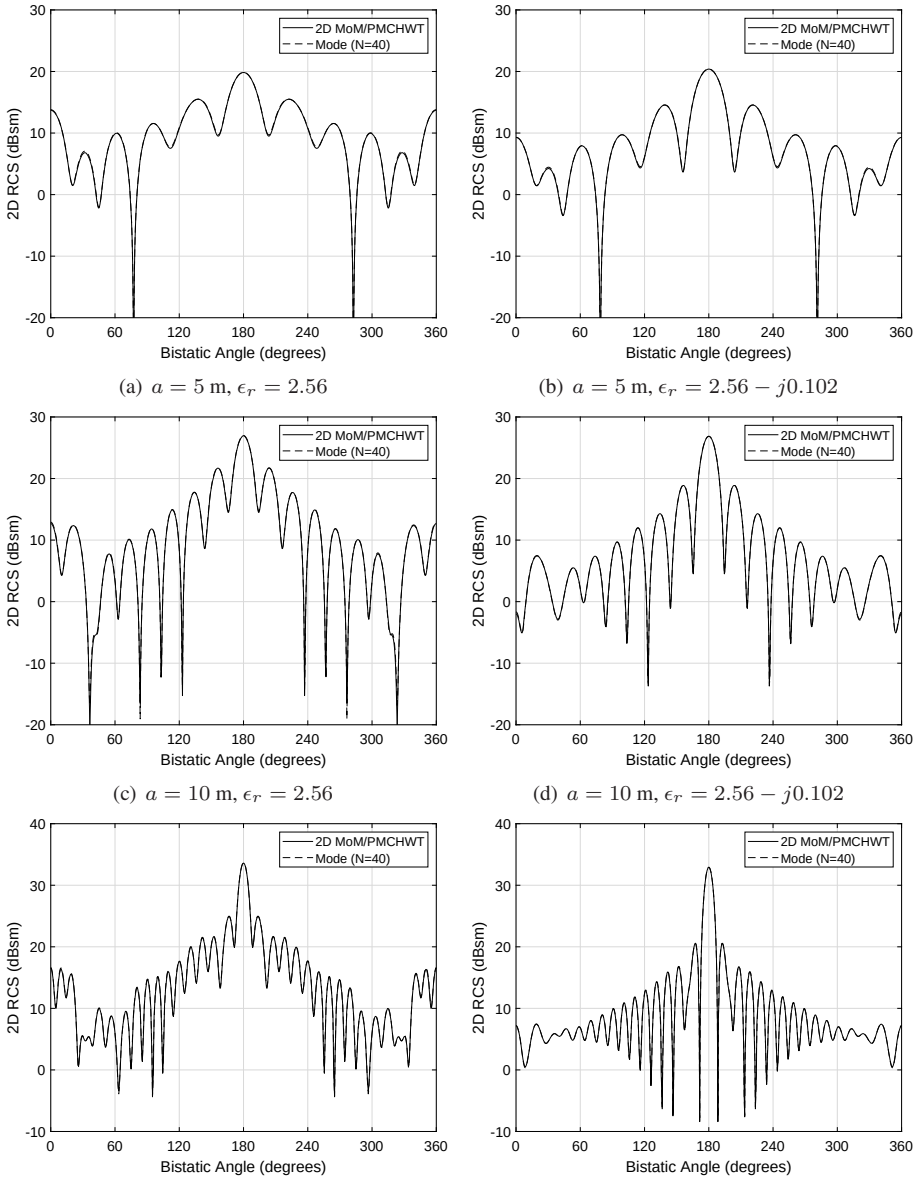
$$V^{H,t} = V^H\left(\mathbf{g}^t_{S_{01}}, R_0\right) , \tag{6.154}$$

where the notation $\mathrm{X}\left(\mathbf{a}_{S_{mn}}, R_l\right)$ similarly indicates that X is evaluated in R_l using the testing functions $\mathbf{a}_{S_{mn}}$. Finally, $J^z_{S_{01}}$ and $M^t_{S_{01}}$ are the coefficients of the electric and magnetic basis functions in the solution vector, respectively, on S_{01}.

6.2.9.1.3 Results

We consider cylinders of radius $a = 5$, 10, and 20 meters, first with $\epsilon_r = 2.56$ (lossless) and then with $\epsilon_r = 2.56 - j0.102$ (lossy). Setting $k_0 = 1$, we compute the bistatic RCS for $0 \leq \phi^s \leq 2\pi$ with $\phi^i = 0$. For the MoM we use 10 segments per free space wavelength on the boundary, with a minimum of 64 segments, and for the modal solution, $N = 40$. The MoM results are compared to the modal solution in Figure 6.16. The agreement is excellent in all cases. We next compute the RCS in the backscattering and forward-scattering directions for $0 < k_0 a \leq 40$. The MoM uses the same parameters as before, and for the modal solution $N = 60$. For comparison against the data plotted in Figures (4-7)(a) and (4-9)(a) in [3], the RCS has been normalized with respect to πa. The agreement is again seen to be very good.

To determine the near fields in R_0 and R_1, we can use (3.120) and (3.122) and integrate the MoM currents on S_{01} for points in R_0 and in R_1, using the appropriate vector orientations and material parameters in each region. In Figure 6.19a is shown the scattered near electric field in R_0 (in V/m) for a lossless dielectric cylinder with radius 1λ and $\epsilon_1 = 2.56$. In Figure 6.19b are shown the total fields, where in R_0 the field is the sum of the incident and scattered electric field, and in R_1 it is the transmitted field. We see that the total fields are continuous across the dielectric boundary.



(a) $a = 5$ m, $\epsilon_r = 2.56$

(b) $a = 5$ m, $\epsilon_r = 2.56 - j0.102$

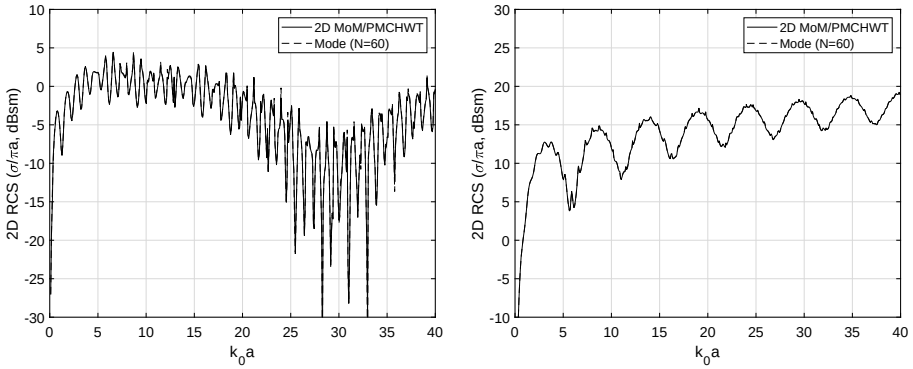
(c) $a = 10$ m, $\epsilon_r = 2.56$

(d) $a = 10$ m, $\epsilon_r = 2.56 - j0.102$

(e) $a = 20$ m, $\epsilon_r = 2.56$

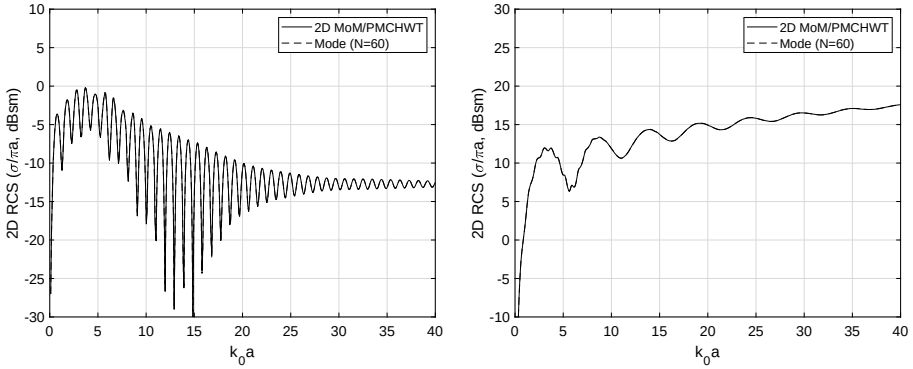
(f) $a = 20$ m, $\epsilon_r = 2.56 - j0.102$

Figure 6.16: 2D Dielectric Cylinder: Bistatic RCS, TM Polarization



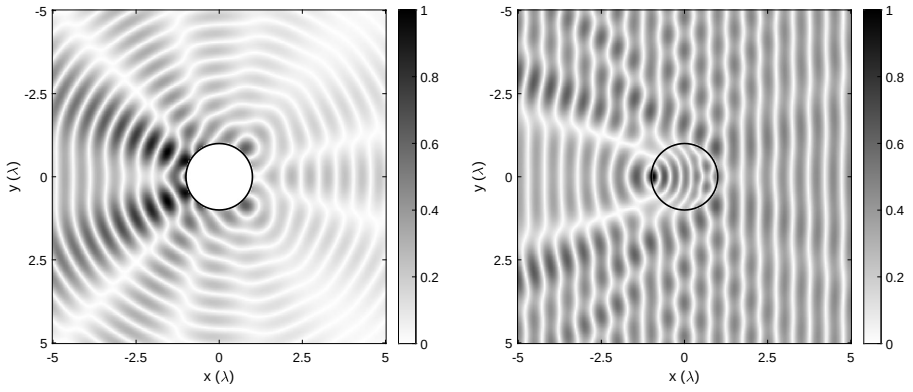
(a) Backscattering ($\phi^s = 0$) (b) Forward Scattering ($\phi^s = \pi$)

Figure 6.17: 2D Lossless Dielectric Cylinder: RCS versus Radius, TM Polarization



(a) Backscattering ($\phi^s = 0$) (b) Forward Scattering ($\phi^s = \pi$)

Figure 6.18: 2D Lossy Dielectric Cylinder: RCS versus Radius, TM Polarization



(a) Scattered Near Field ($|\mathbf{E}^s|$, V/m) (b) Total Near Field ($|\mathbf{E}^{tot}|$, V/m)

Figure 6.19: 2D Dielectric Cylinder: TM Near Fields for $\phi^i = 0$

6.2.9.1.4 Dielectric Cylinder: TE Polarization

For the exact modal solution of a dielectric cylinder, the series coefficients B_n for TE polarization are [3]

$$B_n = -\frac{(k_1/\epsilon_1)J_n(k_0a)J_n'(k_1a) - (k_0/\epsilon_0)J_n'(k_0a)J_n(k_1a)}{(k_1/\epsilon_1)H_n^{(2)}(k_0a)J_n'(k_1a) - (k_0/\epsilon_0)H_n'^{(2)}(k_0a)J_n(k_1a)}\,, \tag{6.155}$$

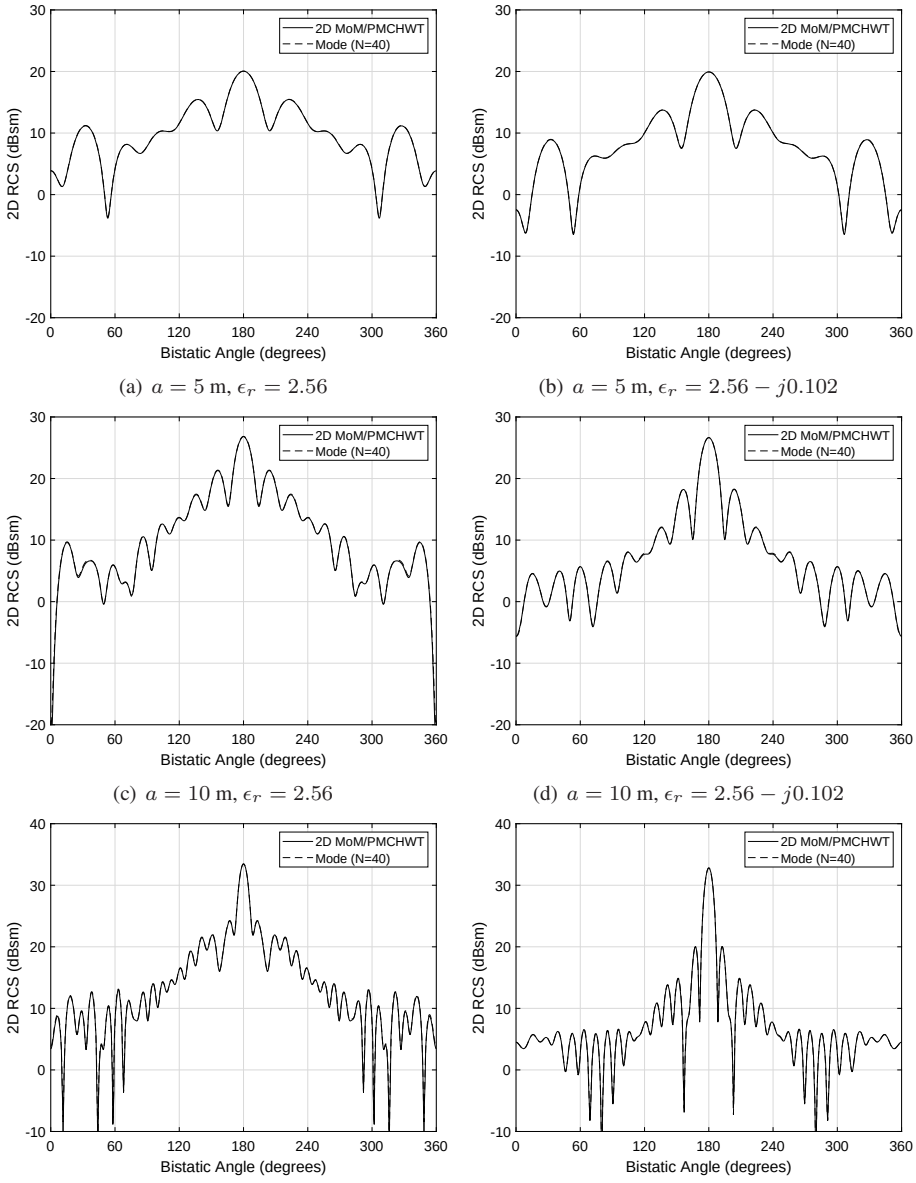
where the scattered field is given by (6.102).

6.2.9.1.5 MoM Linear System

For the TE case, the MoM linear system is obtained from (6.148) by simply interchanging the z and t superscripts.

6.2.9.1.6 Results

We consider the same examples presented in Section 6.2.9.1.1, but for TE polarization. The discretization and other parameters remain identical. The results are shown in Figures 6.20–6.23. The comparisons between the MoM and modal solutions are again very good. For comparison against the data plotted in Figures (4-7)(b) and (4-9)(b) in [3], the RCS in Figures 6.21 and 6.22 has been normalized with respect to πa.



(a) $a = 5$ m, $\epsilon_r = 2.56$

(b) $a = 5$ m, $\epsilon_r = 2.56 - j0.102$

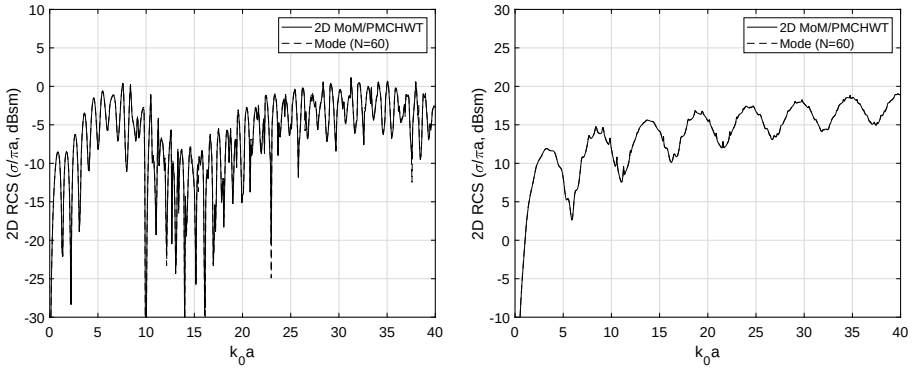
(c) $a = 10$ m, $\epsilon_r = 2.56$

(d) $a = 10$ m, $\epsilon_r = 2.56 - j0.102$

(e) $a = 20$ m, $\epsilon_r = 2.56$

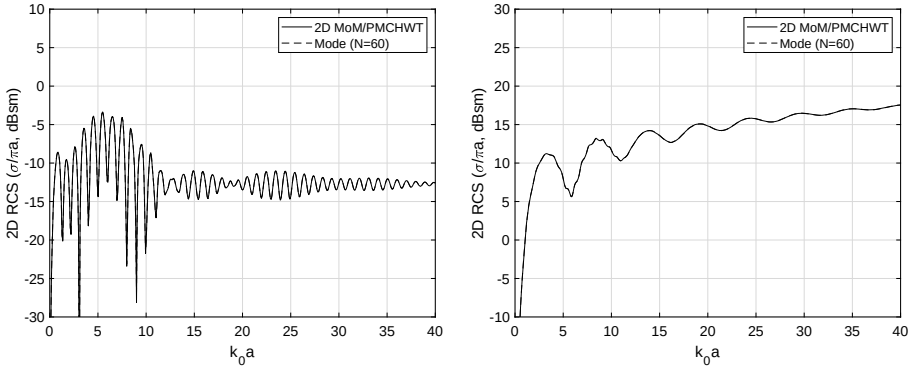
(f) $a = 20$ m, $\epsilon_r = 2.56 - j0.102$

Figure 6.20: 2D Dielectric Cylinder: Bistatic RCS, TE Polarization



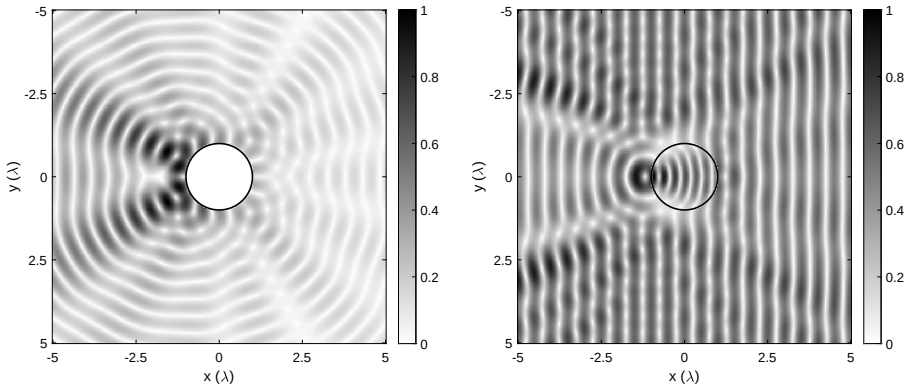
(a) Backscattering ($\phi^s = 0$) (b) Forward Scattering ($\phi^s = \pi$)

Figure 6.21: 2D Lossless Dielectric Cylinder: RCS versus Radius, TE Polarization



(a) Backscattering ($\phi^s = 0$) (b) Forward Scattering ($\phi^s = \pi$)

Figure 6.22: 2D Lossy Dielectric Cylinder: RCS versus Radius, TE Polarization



(a) Scattered Near Field ($|\mathbf{E}^s|$, V/m) (b) Total Near Field ($|\mathbf{E}^{tot}|$, V/m)

Figure 6.23: 2D Dielectric Cylinder: TE Near Fields For $\phi^i = 0$

6.2.9.2 Coated Cylinder

We next consider a conducting cylinder of radius a_1 with a dielectric coating of thickness d, giving an outermost radius of $a_0 = a_1 + d$. This problem has three regions: the PEC region R_2, the dielectric region R_1, and the exterior free space region R_0. There are two interfaces: the inner conducting interface S_{12} with radius a_1, and the outer dielectric interface S_{01} with radius a_0. In this case, we test the EFIE and MFIE on S_{01}, and the CFIE on S_{12}.

6.2.9.2.1 Coated Cylinder: TM Polarization

For the exact modal solution of a coated cylinder, the series coefficients A_n for TM polarization are [3]

$$A_n = -\frac{J_n(k_0 a_0) - iZ_n J_n'(k_0 a_0)}{H_n^{(2)}(k_0 a_0) - iZ_n H_n'^{(2)}(k_0 a_0)} \,, \tag{6.156}$$

where

$$iZ_n = \frac{k_0 \mu_1}{k_1 \mu_0} \left[\frac{J_n(k_1 a_0) H_n^{(2)}(k_1 a_1) - H_n^{(2)}(k_1 a_0) J_n(k_1 a_1)}{J_n'(k_1 a_0) H_n^{(2)}(k_1 a_1) - H_n'^{(2)}(k_1 a_0) J_n(k_1 a_1)} \right] . \tag{6.157}$$

6.2.9.2.2 MoM Linear System

For the TM case, the MoM linear system can be written in block form as

$$\begin{bmatrix} Z_{11}^{zz} & Z_{12}^{zz} & Z_{13}^{zt} \\ Z_{21}^{zz} & Z_{22}^{zz} & Z_{23}^{zt} \\ Z_{31}^{tz} & Z_{32}^{tz} & Z_{33}^{tt} \end{bmatrix} \begin{bmatrix} J_{S_{01}}^{z} \\ J_{S_{12}}^{z} \\ M_{S_{01}}^{t} \end{bmatrix} = \begin{bmatrix} V^{E,z} \\ 0 \\ V^{H,t} \end{bmatrix} , \tag{6.158}$$

where the matrix blocks are

$$Z_{11}^{zz} = \frac{\omega \mu_0}{4} \mathrm{L}^{zz}\big(\mathbf{f}_{S_{01}}^{z}, \mathbf{f}_{S_{01}}^{z}, R_0\big) + \frac{\omega \mu_1}{4} \mathrm{L}^{zz}\big(\mathbf{f}_{S_{10}}^{z}, \mathbf{f}_{S_{10}}^{z}, R_1\big) \,, \tag{6.159}$$

$$Z_{12}^{zz} = \frac{\omega \mu_1}{4} \mathrm{L}^{zz}\big(\mathbf{f}_{S_{10}}^{z}, \mathbf{f}_{S_{12}}^{z}, R_1\big) \,, \tag{6.160}$$

$$Z_{13}^{zt} = \mathrm{K}^{zt}\big(\mathbf{f}_{S_{01}}^{z}, \mathbf{g}_{S_{01}}^{t}, R_0\big) + \mathrm{K}^{zt}\big(\mathbf{f}_{S_{10}}^{z}, \mathbf{g}_{S_{10}}^{t}, R_1\big) \,, \tag{6.161}$$

$$Z_{21}^{zz} = \alpha \frac{\omega \mu_1}{4} \mathrm{L}^{zz}\big(\mathbf{f}_{S_{12}}^{z}, \mathbf{f}_{S_{10}}^{z}, R_1\big) + (1-\alpha)\eta_1 \mathrm{nK}^{zz}\big(\mathbf{f}_{S_{12}}^{z}, \mathbf{f}_{S_{10}}^{z}, R_1\big) \,, \tag{6.162}$$

$$Z_{22}^{zz} = \alpha \frac{\omega \mu_1}{4} \mathrm{L}^{zz}\big(\mathbf{f}_{S_{12}}^{z}, \mathbf{f}_{S_{12}}^{z}, R_1\big) + (1-\alpha)\eta_1 \mathrm{nK}^{zz}\big(\mathbf{f}_{S_{12}}^{z}, \mathbf{f}_{S_{12}}^{z}, R_1\big) \,, \tag{6.163}$$

$$Z_{23}^{zt} = \alpha \mathrm{K}^{zt}\big(\mathbf{f}_{S_{12}}^{z}, \mathbf{g}_{S_{10}}^{t}, R_1\big) + (1-\alpha)\eta_1 \frac{\omega \epsilon_1}{4} \mathrm{nL}^{zt}\big(\mathbf{f}_{S_{12}}^{z}, \mathbf{g}_{S_{10}}^{t}, R_1\big) \,, \tag{6.164}$$

$$Z_{31}^{tz} = -\mathrm{K}^{tz}\big(\mathbf{g}_{S_{01}}^{t}, \mathbf{f}_{S_{01}}^{z}, R_0\big) - \mathrm{K}^{tz}\big(\mathbf{g}_{S_{10}}^{t}, \mathbf{f}_{S_{10}}^{z}, R_1\big) \,, \tag{6.165}$$

$$Z_{32}^{tz} = -\mathrm{K}^{tz}\big(\mathbf{g}_{S_{10}}^{t}, \mathbf{f}_{S_{12}}^{z}, R_1\big) \,, \tag{6.166}$$

$$Z_{33}^{tt} = \frac{\omega \epsilon_0}{4} \mathrm{L}^{tt}\big(\mathbf{g}_{S_{01}}^{t}, \mathbf{g}_{S_{01}}^{t}, R_0\big) + \frac{\omega \epsilon_1}{4} \mathrm{L}^{tt}\big(\mathbf{g}_{S_{10}}^{t}, \mathbf{g}_{S_{10}}^{t}, R_1\big) \,, \tag{6.167}$$

and $J^z_{S_{01}}$ and $J^z_{S_{12}}$ are the coefficients of the electric basis functions on S_{01} and S_{12}, respectively, and $M^t_{S_{01}}$ are the coefficients of the magnetic basis functions on S_{01}. The right-hand side matrix blocks are

$$V^{E,z} = V^E\left(\mathbf{f}^z_{S_{01}}, R_0\right) \ , \tag{6.168}$$

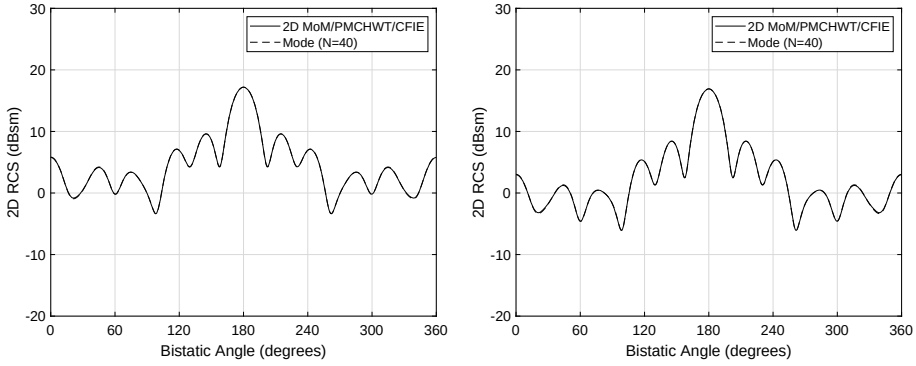
$$V^{H,t} = V^H\left(\mathbf{g}^t_{S_{01}}, R_0\right) \ . \tag{6.169}$$

6.2.9.2.3 Results

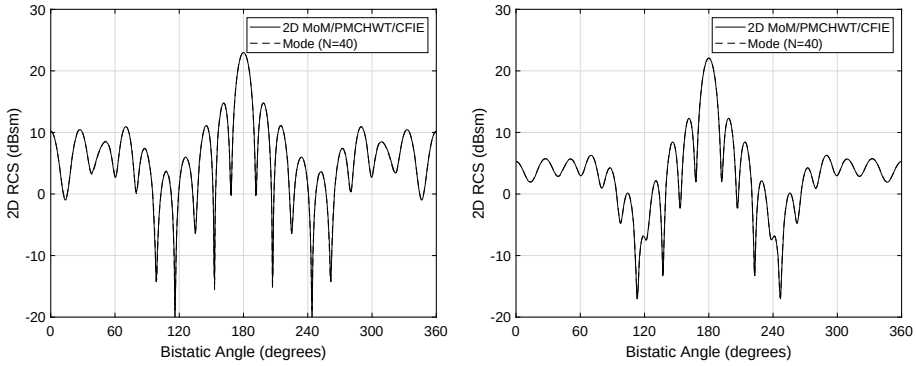
First, we consider coated cylinders with $(a_0, a_1) = (5\lambda, 2.5\lambda)$, $(a_0, a_1) = (10\lambda, 5\lambda)$, and $(a_0, a_1) = (20\lambda, 10\lambda)$. For each, we will consider a lossless coating ($\epsilon_r = 2.56$) and then a lossy coating ($\epsilon_r = 2.56 - j0.102$). We compute the bistatic RCS for $0 \leq \phi^s \leq 2\pi$ with $\phi^i = 0$. For the MoM we use 10 segments per free space wavelength on the boundary, with a minimum of 64 segments. On the inner conducting boundary, we apply the CFIE ($\alpha = 0.5$), and PMCHWT is applied on the outer dielectric boundary. For the modal solution, $N = 40$. The MoM results are compared to the modal solution in Figure 6.24. The agreement is good in all cases.

We next compute the near fields for a coated cylinder with $(a_0, a_1) = (2.5\lambda, 1\lambda)$, and a lossless coating ($\epsilon_r = 2.56$), for $\phi^i = 0$. To determine the near fields in R_0 and R_1, we can use (3.120) and (3.122) and integrate the MoM currents on S_{01} for the field in R_0, and the currents on S_{01} and S_{12} for the field in R_1, using the appropriate vector orientations and material parameters in each region. In Figure 6.25a is shown the normalized scattered near electric field in R_0 (in V/m). In Figure 6.25b are shown the normalized total fields, where in R_0 the field is the sum of the incident and scattered electric field, and in R_1 it is the transmitted field.

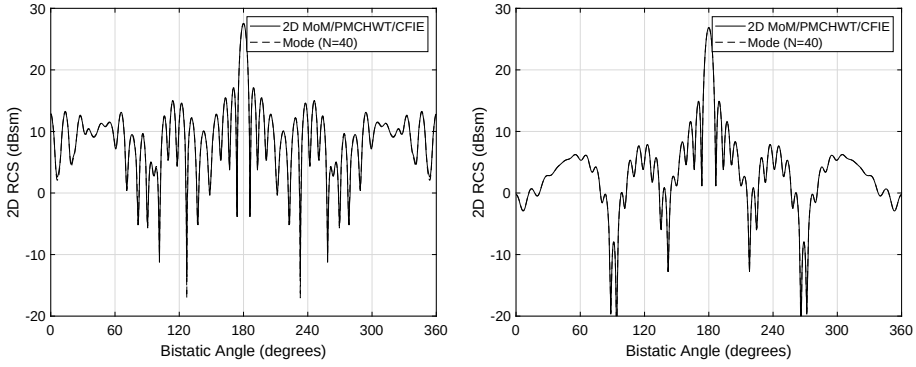
We next analyze a coated cylinder where $a_0 = 1.1a_1$. Setting $k_0 = 1$, we compute the RCS in the backscattering and forward-scattering directions for $0 < k_0 a \leq 40$. For the MoM solution, both interfaces are discretized using 10 points per λ_0 with a minimum of 64 segments on each, and for the modal solution, $N = 60$. The MoM results are compared to the modal solution for a lossless ($\epsilon_r = 2.56$) and lossy ($\epsilon_r = 2.56 - j0.102$) coating in Figures 6.26 and 6.27, respectively. The RCS has again been normalized with respect to πa.



(a) $(a_0, a_1) = (5\lambda, 2.5\lambda)$, $\epsilon_r = 2.56$ (b) $(a_0, a_1) = (5\lambda, 2.5\lambda)$, $\epsilon_r = 2.56 - j0.102$

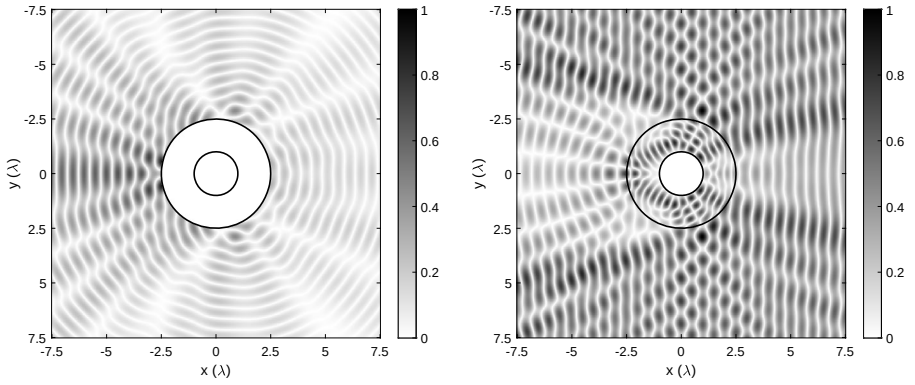


(c) $(a_0, a_1) = (10\lambda, 5\lambda)$, $\epsilon_r = 2.56$ (d) $(a_0, a_1) = (10\lambda, 5\lambda)$, $\epsilon_r = 2.56 - j0.102$



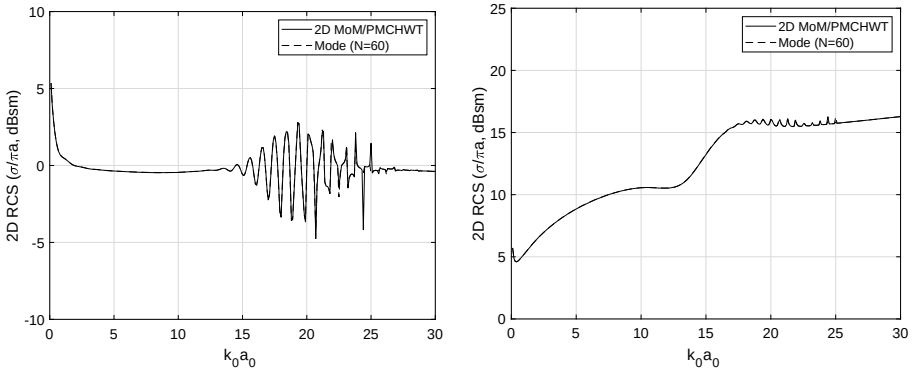
(e) $(a_0, a_1) = (20\lambda, 10\lambda)$, $\epsilon_r = 2.56$ (f) $(a_0, a_1) = (20\lambda, 10\lambda)$, $\epsilon_r = 2.56 - j0.102$

Figure 6.24: 2D PEC Cylinder with Coating: Bistatic RCS, TM Polarization



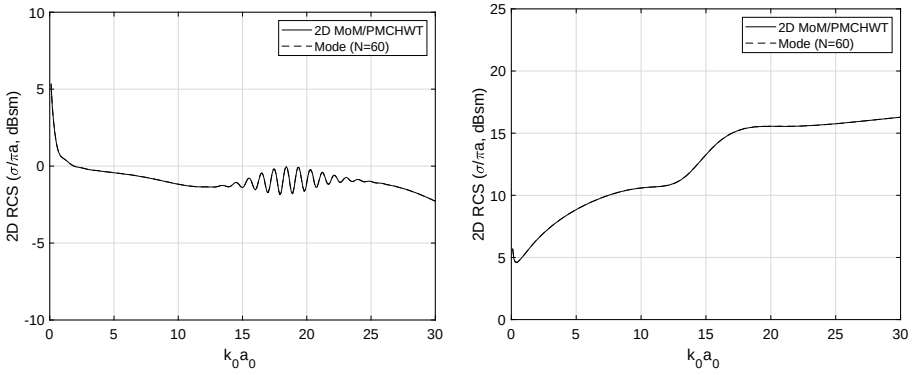
(a) Scattered Near Field ($|\mathbf{E}^s|$, V/m) (b) Total Near Field ($|\mathbf{E}^{tot}|$, V/m)

Figure 6.25: 2D PEC Cylinder with Lossless Coating: TM Near Fields for $\phi^i = 0$



(a) Backscattering ($\phi^s = 0$) (b) Forward Scattering ($\phi^s = \pi$)

Figure 6.26: 2D PEC Cylinder with Lossless Coating: RCS versus $k_0 a$, TM Polarization



(a) Backscattering ($\phi^s = 0$) (b) Forward Scattering ($\phi^s = \pi$)

Figure 6.27: 2D PEC Cylinder with Lossy Coating: RCS versus $k_0 a$, TM Polarization

6.2.9.2.4 Coated Cylinder: TE Polarization

For the exact modal solution of a coated cylinder, the series coefficients B_n for TE polarization are [3]

$$B_n = -\frac{J_n(k_0 a_0) - iY_n J_n'(k_0 a_0)}{H_n^{(2)}(k_0 a_0) - iY_n H_n'^{(2)}(k_0 a_0)}\,, \tag{6.170}$$

where

$$iY_n = \frac{k_0 \epsilon_1}{k_1 \epsilon_0}\left[\frac{J_n(k_1 a_0) H_n'^{(2)}(k_1 a_1) - H_n^{(2)}(k_1 a_0) J_n'(k_1 a_1)}{J_n'(k_1 a_0) H_n'^{(2)}(k_1 a_1) - H_n'^{(2)}(k_1 a_0) J_n'(k_1 a_1)}\right]. \tag{6.171}$$

6.2.9.2.5 MoM Linear System

For the TE case, the MoM linear system is obtained from (6.158) by simply interchanging the z and t superscripts.

6.2.9.2.6 Results

We consider the same examples presented in Section 6.2.9.2.1, but for TE polarization. The discretization and other parameters remain identical. The results are shown in Figures 6.28–6.31. The comparisons between the MoM and modal solutions are again very good.

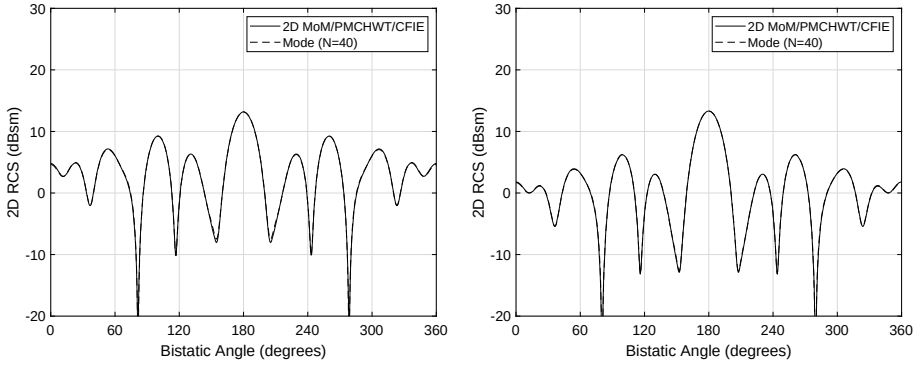
References

[1] *The Integrator*. Wolfram Research, integrals.wolfram.com.

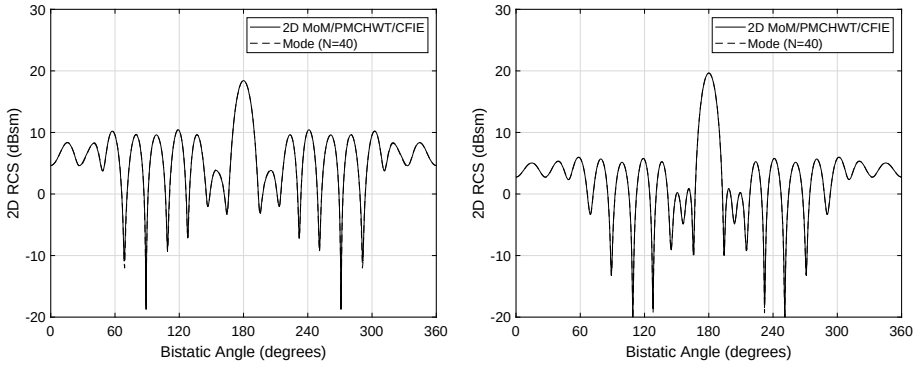
[2] M. Abramowitz and I. Stegun, *Handbook of Mathematical Functions*. National Bureau of Standards, 1966.

[3] G. T. Ruck, ed., *Radar Cross Section Handbook*. Plenum Press, 1970.

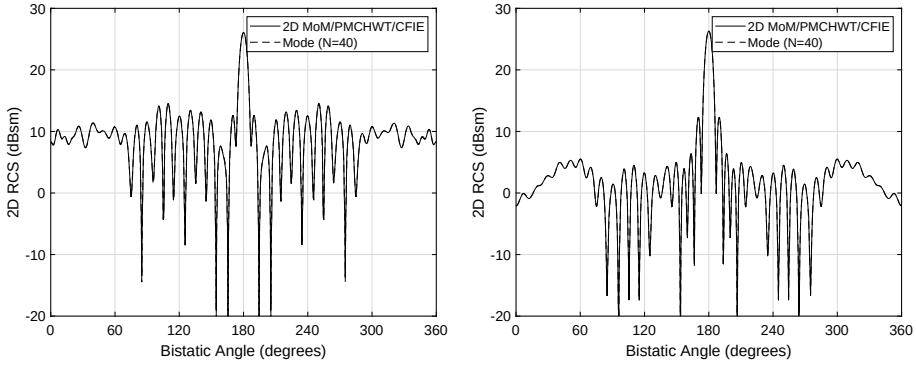
[4] L. N. Medgyesi-Mitschang and J. M. Putnam, "Electromagnetic scattering from axially inhomogeneous bodies of revolution," *IEEE Trans. Antennas Propagat.*, vol. 32, pp. 796–806, March 1984.



(a) $(a_0, a_1) = (5\lambda, 2.5\lambda)$, $\epsilon_r = 2.56$ (b) $(a_0, a_1) = (5\lambda, 2.5\lambda)$, $\epsilon_r = 2.56 - j0.102$

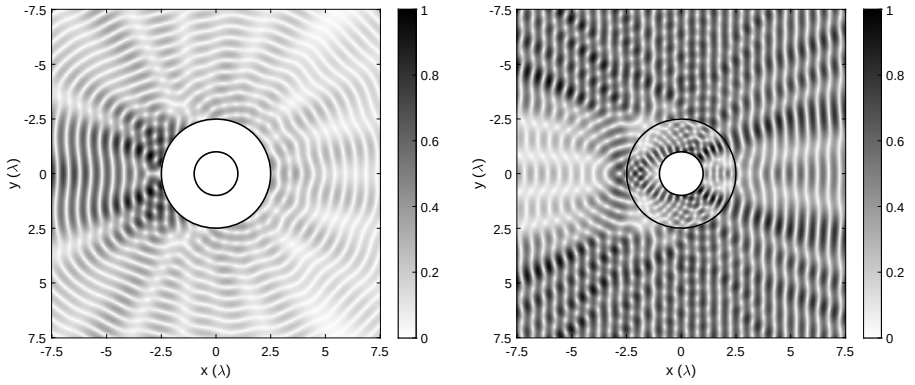


(c) $(a_0, a_1) = (10\lambda, 5\lambda)$, $\epsilon_r = 2.56$ (d) $(a_0, a_1) = (10\lambda, 5\lambda)$, $\epsilon_r = 2.56 - j0.102$



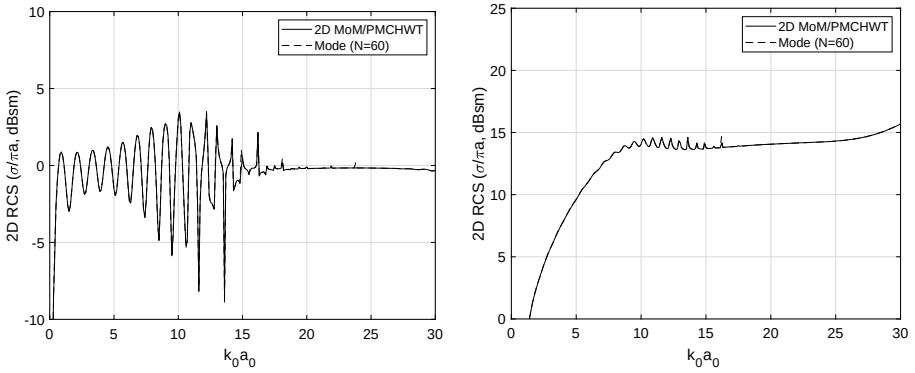
(e) $(a_0, a_1) = (20\lambda, 10\lambda)$, $\epsilon_r = 2.56$ (f) $(a_0, a_1) = (20\lambda, 10\lambda)$, $\epsilon_r = 2.56 - j0.102$

Figure 6.28: 2D PEC Cylinder with Coating: Bistatic RCS, TE Polarization



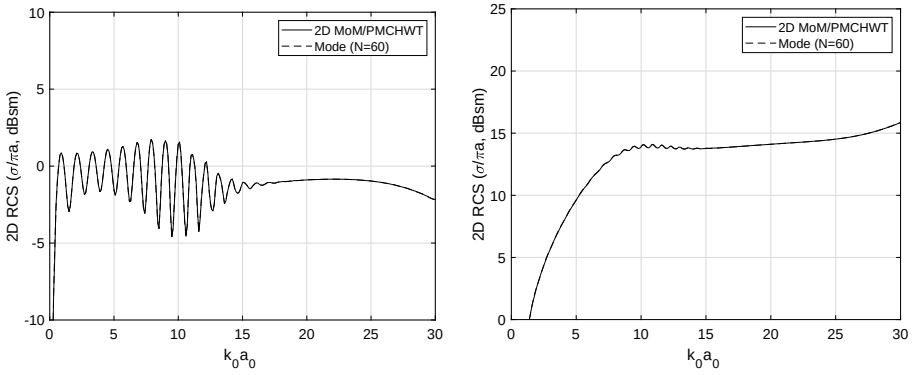
(a) Scattered Near Field ($|\mathbf{E}^s|$, V/m) (b) Total Near Field ($|\mathbf{E}^{tot}|$, V/m)

Figure 6.29: 2D PEC Cylinder with Lossless Coating: TE Near Fields for $\phi^i = 0$



(a) Backscattering ($\phi^s = 0$) (b) Forward Scattering ($\phi^s = \pi$)

Figure 6.30: 2D PEC Cylinder with Lossless Coating: RCS versus $k_0 a$, TE Polarization



(a) Backscattering ($\phi^s = 0$) (b) Forward Scattering ($\phi^s = \pi$)

Figure 6.31: 2D PEC Cylinder with Lossy Coating: RCS versus $k_0 a$, TE Polarization